DIFFUSION-ATTENUATED MR SIGNAL FOR PARTICLES SUBJECT TO FORCES OR IN DISORDERED MEDIA

by

Kadir Şimşek

B.S., Physics, Boğaziçi University, 2014

Submitted to the Institute for Graduate Studies in
Science and Engineering in partial fulfillment of
the requirements for the degree of
Master of Science

Graduate Program in Physics

Boğaziçi University

2017

DIFFUSION-ATTENUATED MR SIGNAL FOR PARTICLES SUBJECT TO FORCES OR IN DISORDERED MEDIA

APPROVED BY:

Prof. Dr. Mehmet Burçin Ünlü .....
(Thesis Supervisor)

Assoc. Prof. Özhan Özatay .....

Assist. Prof. Evren Özarslan .....

DATE OF APPROVAL: 18.07.2017

ACKNOWLEDGEMENTS

I would first like to thank my thesis advisor Prof. M. Burçin Ünlü for providing me an opportunity to study one of his research labs as well as his guidance. I would also like to express my sincere gratitude to Assist. Prof. Evren Özarslan of the Department of Biomedical Engineering at Linköping University for his admirable mentoring on my master study with his profound knowledge.

I would also like to thank my fellow colleagues Erkam and Serhat for their support and friendship along the years of my master education. I would also thank to my friend Adnan for motivating me spiritually throughout writing my thesis.

ABSTRACT

DIFFUSION-ATTENUATED MR SIGNAL FOR PARTICLES SUBJECT TO FORCES OR IN DISORDERED MEDIA

Magnetic resonance imaging (MRI) have been advanced significantly since its discovery, especially in imaging soft biological structures. One of the most studied and improved technique in this field is diffusion MRI consisting of two methods; namely, diffusion weighted imaging (DWI) and diffusion tensor imaging (DTI). This imaging modality is rather regarded with imaging tissues in micro environments,where restricted diffusion occurs, such as neural networks and microscopically crowded media . In this thesis, we will investigate the influence of diffusion on nuclear magnetic resonance (NMR) experiments in two distinct parts. Firstly, we will study the NMR signal measured from molecules diffusing under the influence of a parabolic (Hookean) potential. We will induce a Hookean potential into the free diffusion state to restrict the random movements of the molecules. Then, a recently introduced method, confinement tensor model, is employed in the analytical measurements to validate the random walk simulations. The second part consists of rather a different investigation regarding the determination of energy landscapes of boundaries in which water molecules undergo random walk. A recently proposed pulse sequence, allowing us to perform an inverse Fourier transformation on the signal, is employed to image the potential energy landscape in which the water molecules diffuse. The energy landscape encodes information about heterogeneities of a domain as well as adhesiveness feature of boundaries. As an additional approach, we will give a brief discussion about the fractional Brownian motion (fBm) to bring more realistic perspective to the diffusive motion of the particles in restricted regions.

ÖZET

KUVVETLERE MARUZ KALAN YADA BOZUK ORTAMLARDA BULUNAN PARÇACIKLAR İÇİN DİFÜZYON-SÖNÜMLÜ MR SİNYALİ

Manyetik rezonans görüntüleme (MRI), özellikle yumuşak biyolojik yapıların görüntülenmesinde, keşfedildiğinden beri önemli ölçüde gelişim kat etmiştir. Bu alanda en çok çalışılan ve geliştirilen tekniklerden biri, difüzyon MR görüntüsüdür. Bu görüntüleme modeli, sinir ağları ve mikroskopik olarak kalabalık ortamlar gibi kısıtlı difüzyonun gerçekleştiği mikro ortamlardaki dokuları görüntülemeye zemin hazırlamaktadır. Bu tezde, difüzyonun nükleer manyetik rezonans (NMR) deneyleri üzerindeki etkisini iki ayrı bölümde inceleyeceğiz. Öncelikle, parabolik (Hookean) potansiyelin etkisi altında yayılmış moleküllerden ölçülen NMR sinyalini hesaplayacağız. Moleküllerin rastgele hareketlerini kısıtlamak için serbest difüzyon durumuna bir parabolik potansiyeli yükleyeceğiz. Ardından, rasgele yürüyüş simülasyonlarını doğrulamak için analitik ölçümlerde yakın zamanda tanıtılan bir yöntem olan sınırlayıcı tensör modelini kullanacağız. İkinci bölüm, su moleküllerinin rasgele yürüdüğü, sınırların enerji haritalarını belirlenmesine ilişkin farklı bir araştırmadan oluşmaktadır. Sinyal üzerinde bir ters Fourier dönüşümü gerçekleştirmemize izin veren yakın zamanda önerilen bir nabız dizisi, su moleküllerinin içinde bulunduğu potansiyel enerji haritasını görüntülemek için kullanacağız. Enerji haritası bir ortamın heterojenlikleri ve sınırlarının yapışkan özelliği hakkında bilgi verir. Ek bir yaklaşım olarak, kısıtlı bölgelerdeki parçacıkların difüzyon hareketine daha fazla gerçeklik kazandırmak için fraksiyonel Brown hareketi (fBm) hakkında kısa bir çalışma yapacağız.

TABLE OF CONTENTS

LIST OF FIGURES

LIST OF SYMBOLS

$\mathbf{B}$	Total magnetic field
$\mathbf{B}_0$	Main magnetic field
$\mathbf{B}_1$	Applied RF field
$\mathbf{B}_{eff}$	Effective magnetic field
$\mathbf{C}$	Confinement Tensor
D	Diffusivity constant
D_0	Bulk diffusivity constant
$\mathbf{G}$	Applied magnetic gradient field
$\mathcal{G}$	Propagator for diffusion equation
$\mathbf{L}$	Macroscopic angular momentum
l	Step length of particles
$\mathbf{M}(t)$	Macroscopic magnetization
$\mathbf{M}_0$	Initial magnetization
$\mathbf{M}_{xy}$	Transverse magnetization
$\mathbf{M}_z$	Longitudinal magnetization
N	Number of spins or steps
P_D	Proton density
S	NMR signal measurement
T_1	Relaxation time of longitudinal magnetization
T_2	Relaxation time of transverse magnetization
T_E	Echo time
T_I	Inversion time
T_R	Repetition time
α	RF pulse angle
γ	Gyromagnetic ratio
Γ	Gamma function
δ	Application duration of gradient field
Δ	Diffusion time

$\boldsymbol{\mu}$	Magnetic moment
σ_x	Mean squared displacement of x
τ	Step time of particles
υ	Stochastic speed parameter
ϕ	Accumulated Phase
$\mathbf{\Phi}$	Microscopic angular momentum
ω	Larmor frequency
$\mathbf{\Omega}$	Inverse time

LIST OF ACRONYMS/ABBREVIATIONS

1D	One Dimensional
2D	Two Dimensional
3D	Three Dimensional
ADC	Apparent Diffusion Coefficient
C	Carbon
CSF	Cerebrospinal fluid
CT	Computed Tomography
CTRW	Continuous Time Random Walk
DWI	Diffusion Weighted Imaging
DTI	Diffusion Tensor Imaging
EAP	Ensemble Average Propagator
EPI	Echo Planar Imaging
ETSE	Echo Train Spin Echo
FA	Fractional Anisotropy
fBm	Fractional Brownian Motion
FLAIR	Fluid Attenuation Inversion Recovery
FOV	Field of View
FID	Free Induction Decay
GM	Gray Matter
IR	Inversion Recovery
ISMRM	International Society for Magnetic Resonance in Medicine
IVIM	Intravoxel Incoherent Motion
MCF	Multiple Correlation Function
MRI	Magnetic Resonance Imaging
MSD	Mean Squared Displacement
n-fBm	nth Order Fractional Brownian Motion
NMR	Nuclear Magnetic Resonance
O_2	Oxygen

ppm	Parts per million
RA	Relative Anisotropy
RF	Radio Frequency
RARE	Rapid Acquisition and Rapid Enhancement
SNR	Signal to Noise Ratio
STIR	Short Tau Inversion Recovery
WM	White Matter

1. INTRODUCTION

Among all other medical imaging techniques, such as Computed Tomography (CT), X-Ray, and Ultrasound, Magnetic Resonance Imaging (MRI) is undoubtedly the most extensible and remarkable imaging technology. Through capability of establishing dynamic physiologic variations and illustrating tomographic 3D soft tissue images, MRI provides a delicate tissue contrast of high spatial resolution. Generating images requires an immense physical data set which is subject to the physics of nuclear magnetic resonance (NMR). Reconstructing NMR images can be performed in various acquisition techniques, for instance T1 and T2 relaxation processes [3–5], variations in tissue susceptibility [6–8], diffusion MRI [9–12] and image contrast [13]. Signal strength measured from a tissue can be adjusted to be different from another tissue so that there can be a higher signal, a lower signal and even no signal at all. All these possibilities is a result of the physics behind this modality, which is completely different from other imaging methods.

Despite having "nuclear" term in its name, NMR does not utilize its radiation directly for obtaining images. Alternatively, the electromagnetic radiation is a component of the process in NMR, which also consists of a much lower frequency and is not attenuated by tissue, conversely to the X-ray and CT whose high-frequency radiation exposes the organs and then the attenuated radiation is detected. The main concern, in NMR, is the interaction between atomic nuclei and a strong magnetic field. Since the number of hydrogen nuclei is plentiful in organisms, it is much more convenient to measure the signals emitted from the hydrogen nuclei. The obtained signal describes the state of the tissue. Thus, it is significant to have a suitable environment of interest in NMR to differentiate the signals coming from hydrogen nucleus. To acquire all these different aspects of MRI, one needs to understand the fundamental concepts and principles of this imaging technique.

Diffusion MRI is yet another remarkable imaging technique of MRI promising to measure diffusion within tissues in vivo environments [10]. Diffusion weighted imag-

ing (DWI) utilizes the water molecules being subject of diffusion to generate image contrast in MRI [14, 15] In diagnosis of neurological disorders, diffusion MRI provides a substantial benefit and better comprehension of the physiological structure of the brain.

Diffusion weighted NMR signal forms a basis in determining the physical characteristics of biological micro-structures. This makes diffusion NMR a powerful modality to acquire information about the biological environments in which water molecules diffuse. In NMR, the pulse sequences, having a substantial significance in determining regions where diffusion occurs, can manipulate the the sensitivity of NMR signal on diffusion processes [9]. The influence of bulk diffusion on the NMR experiments involving general gradient waveforms have been completely determined [16, 17].

In this thesis, we will study the influence of a parabolic potential on the spin-bearing particles perform a random motion [18] which has been studied statistically [19,20]. Then, we will perform simulations to determine potential energy landscapes of a boundary as well as adhesive property by introducing recently proposed pulsed field gradient sequences [1,2]. The information about the bulk heterogeneities of boundaries is encoded in these energy landscapes. This study will presented at International Society for Magnetic Resonance in Medicine (ISMRM) 2017 conference. Furthermore, the effects of fractional Brownian motion have been considered very well in recent studies [21–23] As an additional study, rather a theoretical one, fractional Brownian motion,the well known example of anomalous diffusion processes, is discussed.

To begin with, let us give a brief discussion about physical background and implementation methods of magnetic resonance imaging (MRI). Then, a short introduction of diffusion and Brownian motion pioneering diffusion MRI modality. Finally, we will demonstrate the simulations and results associated with the aforementioned problems.

2. THEORY

2.1. Nuclear Magnetic Resonance

2.1.1. Physics of Nuclear Magnetic Resonance

NMR is concerned with the nuclei of the atoms. All atoms are formed by protons and neutrons. Regardless of having an odd atomic number or odd mass number, atoms have an angular momentum ($\mathbf{\Phi}$). The spinning charged nucleus generates a microscopic magnetic field in the atom, and such systems are referred as *spin*. Hence, the *magnetization* of a spin can be measured by the magnetic moment of this spin system which is given by,

$$\boldsymbol{\mu} = \gamma \mathbf{\Phi} \tag{2.1}$$

where the γ is the *gyromagnetic ratio* having the units of radian per second tesla and $\gamma = \frac{\gamma}{2\pi}$ has the units of Hz per Tesla.

In substance, there exist millions of nuclei, the magnetic field arising from the spins of these nuclei can be represented as a vector, namely the *net magnetization vector*. The net magnetization vector is zero since all the spin vectors point out random directions. The net magnetization of a substance can be calculated easily by summing up spin magnetization

$$\mathbf{M} = \sum_{n=1}^{N} \boldsymbol{\mu_n} \tag{2.2}$$

where N represents the number of the spins existing in the substance.

The interaction between the spin or and an applied magnetic field ($\mathbf{B}_0$) establishes the fundamentals of NMR. The applied magnetic field (assume to be $\mathbf{B}_0 = B_0\hat{z}$)

makes each magnetic moment ($\boldsymbol{\mu}$) magnetized and parallel with the direction of itself. When all these magnetic moments aligned with the applied magnetic field ($\hat{z}$ axis), the new magnetization vector $\mathbf{M}$ reaches the equilibrium value $\mathbf{M}_0$, the magnitude of which has only spatial dependence ($\vec{r} = (\vec{x}, \vec{y}, \vec{z})$). Whereas, having time dependence of the function $\mathbf{M}$ is very fundamental in NMR and MRI. This function can be manipulated through its spatial dependence by introducing external radio frequency (RF) excitations and magnetic fields while this vector approaches equilibrium value in a main magnetic field. Furthermore, the sample or the substance has a macroscopic *angular momentum* $\mathbf{L}$, comparing to the atomic angular momentum $\mathbf{\Phi}$, which depends on the magnetization of the material or sample, given by

$$\mathbf{M} = \gamma \mathbf{L} \tag{2.3}$$

Applying an external and time varying magnetic field $\mathbf{B}(t)$ makes the magnetic moment $\mathbf{M}(t)$ exposed by a torque which can be described by the equation, namely "the Bloch equation" [24]

$$\frac{\mathrm{d}\mathbf{L}(t)}{\mathrm{d}t} = \mathbf{M}(t) \times \mathbf{B}(t). \tag{2.4}$$

Since the angular momentum $\mathbf{L}$ is related with the magnetization $\mathbf{M}$, we can rewrite the equation (2.4) as

$$\frac{\mathrm{d}\mathbf{M}(t)}{\mathrm{d}t} = \gamma \mathbf{M}(t) \times \mathbf{B}(t). \tag{2.5}$$

The Bloch equation expresses that the net magnetization vector $\mathbf{M}$ precesses around the external magnetic field $\mathbf{B}$ at frequency

$$\omega = \gamma B \tag{2.6}$$

Due to the presence of a strong magnetic field, the net magnetization vector has an equilibrium value leading an emitted signal which is measurable and needed for reconstructing images. To comprehend this emitted signal is originated, one needs to clarify the frequency of precession, namely the *Larmor frequency*, associated with the applied magnetic field. Assume that the magnetization vector $\mathbf{M}$ lies on a plane perpendicular to the main magnetic field $\mathbf{B}$ and $\mathbf{B} = B_0\hat{\mathbf{z}}$. For such system, the magnetization $\mathbf{M}$ precesses in the x-y plane at the Larmor frequency $\omega_0 = \gamma B_0$ where ω_0, is the angular precession frequency, has the units of radians per second $\left(\frac{rad}{s}\right)$.

For a given external magnetic field $\mathbf{B} = B_0\hat{\mathbf{z}}$ and if initially the magnetization $\mathbf{M}(0)$ is oriented at angle α relative to the z-axis, the general solutions of the Bloch equations is given by the equations below;

$$M_x(t) = M_0 \sin\alpha \cos\left(-\omega_0 t + \phi\right) \tag{2.7a}$$

$$M_y(t) = M_0 \sin\alpha \sin\left(-\omega_0 t + \phi\right) \tag{2.7b}$$

$$M_z(t) = M_0 \cos\alpha. \tag{2.7c}$$

For simplicity, before calculating further steps, let us consider the solution for the Bloch equation, having the initial condition $\mathbf{M}(0) = M_0\hat{\mathbf{x}}$ and the external magnetic field $\mathbf{B} = B_0\hat{\mathbf{z}}$, which is given by

$$M_z(t) = 0 \tag{2.8a}$$

$$M_{xy}(t) = M_0 \exp^{-i\omega_0 t} \tag{2.8b}$$

where $M_{xy}(t) = M_x(t) + iM_y(t)$ and $M_0 = M_{xy}(0)$. The magnetization M_0 precesses at frequency $\omega_0 = \gamma B_0$ around B_0.

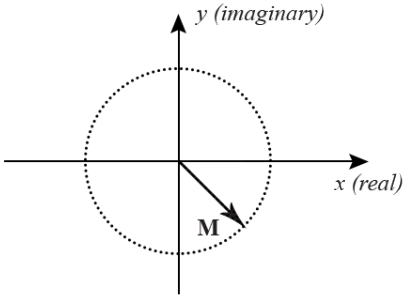

Figure 2.1. The transformation of the magnetization vector **M** in to complex plane illustrates a clear expression for the magnetization.

Moreover, let us improve the case by applying time dependent magnetic field $\mathbf{B}(t) = \mathbf{B}_0 + \mathbf{B}'(t)$. In this case, the Larmor frequency varies with time:

$$\omega(t) = \gamma(B_0 + B'(t)) \tag{2.9}$$

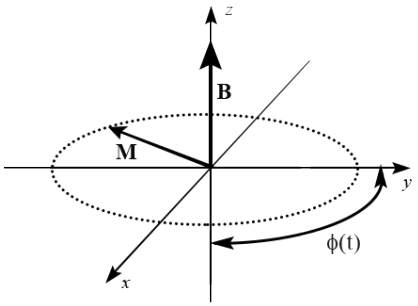

Figure 2.2. The precessing magnetization around the main magnetic field.

The angle $\phi(t)$, describing the phase of the magnetization **M**, can be measured by the integration of the frequency in time:

$$\phi(t) = \gamma \int_0^T (B_0 + B'(t))\,\mathrm{d}t = \omega_0 T + \gamma \int_0^T B'(t)\mathrm{d}t. \tag{2.10}$$

Hence,when we substitute the phase equation (2.10) into the transverse magnetization equation (2.8b), that yields

$$M_{xy}(t) = M_0 e^{-i\left[\omega_0 t + \gamma \int_0^T B'(t)\mathrm{d}t\right]} \tag{2.11}$$

To simplify this equation, one needs to introduce the rotating frame reference. In the coordinate system that we used to observe the magnetization is rotating around the external magnetic field $\mathbf{B}$ at a frequency $\omega_0 = \gamma B_0$. Notably, the magnetization vector $\mathbf{M}$ is rotating about the z-axis that enables us to define new x and y coordinates. By introducing new coordinates, we will make the magnetization vector appear stationary since we transform our reference frame (x, y, z) into a rotating reference frame (x', y', z). The coordinate z remains as the same since it is the reference point.

$$\begin{aligned} \hat{\mathbf{x}}' &= \hat{\mathbf{x}} \cos\omega_0 t + i\hat{\mathbf{y}} \sin\omega_0 t \\ \hat{\mathbf{y}}' &= i\hat{\mathbf{x}} \sin\omega_0 t + \hat{\mathbf{y}} \cos\omega_0 t \\ \hat{\mathbf{z}}' &= \hat{\mathbf{z}} \end{aligned} \tag{2.12}$$

Henceforth, when $\mathbf{B} = B_0\hat{\mathbf{z}}$ the effective magnetic field $\mathbf{B_{eff}}$ in the rotating frame is given by

$$\mathbf{B_{eff}} = \left(B_0 - \frac{\omega_{frame}}{\gamma}\right)\hat{\mathbf{z}} = \left(B_0 - \frac{w_0}{\gamma}\right)\hat{\mathbf{z}} = (B_0 - B_0) = 0 \tag{2.13}$$

Furthermore, the x-y components of the magnetization becomes

$$M_{x'y'}(t) = M_{xy}(t)e^{i\omega_0 t} = M_0. \tag{2.14}$$

The equation (2.14) shows that the magnetization vector becomes stationary in the rotating reference frame. To generalize, when $\mathbf{M} = [M_x, M_y, M_z]$ and $\mathbf{M'} = [M_{x'}, M_{y'}, M_{z'}]$, the transverse magnetization $M_{x'y'}$ and the longitudinal magnetization

$M_{z'}$ in the rotation frame can be expressed as

$$M_{x'y'} = M_{x'} + iM_{y'} = M_{xy}e^{i\omega_0 t} \tag{2.15}$$

$$M_{z'} = M_z. \tag{2.16}$$

Finally, let us consider the time depending magnetic field $\mathbf{B}(t) = [B_0 + B'(t)]\,\hat{\mathbf{z}}$ in the rotating reference frame. The new frequency in the rotating frame is written by

$$\omega'(t) = \gamma\,(B_0 + B'(t)) - \omega_0 = \gamma B'(t) \tag{2.17}$$

and the effective magnetic field in the rotating frame becomes

$$\mathbf{B_{eff}} = \mathbf{B} - \frac{\omega_0}{\gamma}\hat{\mathbf{z}} = (B_0 + B'(t) - B_0)\,\hat{\mathbf{z}} = B'(t)\hat{\mathbf{z}}. \tag{2.18}$$

Using this result in substituting the phase equation (2.10) gives

$$\phi'(t) = \gamma \int_0^T B'(t)\mathrm{d}t \tag{2.19}$$

Before discussing the profound concepts of MRI, it must be explained that the external magnetic field might be varied by the substance or the sample exposed to this field through its *magnetic susceptibility*. Magnetic susceptibility refers to the property of a substance that can change the magnetic field within the substance compared to the surrounding field. *Diamagnetic* substances cause a little decrease in the field whereas *paramagnetic* materials slightly increase the field and *ferromagnetic* ones can lead to a dramatic increase in the field. The presence of a magnetic susceptibility in a magnetic field can be expressed as

$$B_{eff} = B_0(1 + \chi) \tag{2.20}$$

where χ is the *diamagnetic susceptibility* which has a spatial dependent. Since carbon (C) and oxygen (0_2) are diamagnetic, one can consider a human body as showing diamagnetic behavior, resulting in the slight decrease in the field within the body. Also because the diamagnetic susceptibility parameter is spatially dependent, leading sharp changes when measuring the field from inside to outside the body. These severe deviations on the magnetic field could be very significant on acquiring images because of our constant field assumption employed in the image reconstructing equations. However, the variation of the magnetic susceptibility occurs naturally due to the biological activities such as iron accumulation in the brain or oxygen disintegration of hemoglobin in blood which can be extracted in the image [25–28]. Hence, the differences in the susceptibility can have both adverse and beneficial effects in MRI acquisition.

There is one more issue that not only it influences the magnetic field but also the Larmor frequency, that is called the *chemical shift* defined as measuring the change in the Larmor frequency due to the nucleus' chemical environment such as the molecules containing ^{1}H atom. The effect of this phenomenon can be elucidated as the shielding effect of the local electrons on the nucleus that prevents the nucleus from the full exposure of the external magnetic field. Conversely to the susceptibility, chemical shift is very local based and associated with the molecular environment of a nucleus. As a consequence of this feature, the concentration and the position of the molecule that causes chemical shift play a significant role on the spatial effects of it. The change in the magnitude of the main magnetic field represents the chemical shift through this equation

$$B_{eff} = B_0(1 + \zeta) \tag{2.21}$$

where ζ is the *shielding constant* and is a measure of the degree of chemical shift. Then, the associated Larmor frequency yields the shift is given by this equation

$$\omega_{eff} = \omega_0(1 + \zeta) \tag{2.22}$$

Since all molecules might show this intrinsic feature, water, as a reference point is assigned, to measure the chemical shift the molecules produce in parts per million (ppm).

2.1.2. Radio Frequency Excitations

In the most fundamental and clear description, the NMR experiments can be considered as energy transfer. The sample or the substance is subjected to energy at a certain frequency during the experiment. This specific energy will be absorbed by the protons of this sample, and after a short time, when this absorbed energy remitted, it can be detected and processed. A brief representation for the process implicating this absorption and reemission will be argued. Since it will be sufficient to give a general description of this process in this context.

The magnetization vector $\mathbf{M}$ and its manipulation were investigated in the previous section. We have seen that this manipulation on $\mathbf{M}$ forms a basis on the entire magnetic field of NMR, $\mathbf{B}_0$. The simplest way to perform this manipulation requires a short pulse of *radio frequency* (RF) energy, in other words, RF excitation. When the pulse applied, the protons of the sample absorb this energy at a definite frequency and then, a while later, it will be re-emitted at the same frequency. The equation of the Larmor frequency (2.6) shows the relation between the energy at the particular frequency and the magnetic field B_0. We will have a conceptual description of the excitation mechanism. Thus we will only deal with a particular pulse with the resonance condition where the frequency of the pulse is the Larmor frequency.

In a sample, due to the proton number, there is a huge number of absorption and emission process occurring during the RF pulse which constitutes the energy of ω_0 frequency and oriented perpendicular to the main field $\mathbf{B}_0$, denoted as an effective field $\mathbf{B}_1$. The numerous presence of more protons having lower energy results in the net energy absorption by the sample. As a result of effective field's laying on the transverse plane, the magnetization $\mathbf{M}$ and the RF field $\mathbf{B}_1$ couples so that the energy of frequency will be transferred to the protons. This absorption leads to a rotation of

$\mathbf{M}$ that is perpendicular to the both $\mathbf{B}_0$ and $\mathbf{B_1}$. The amplitude and the duration of the RF pulse produce different results, rotation of $\mathbf{M}$ by a tip angle. When $\mathbf{M}$ is rotated into transverse plane entirely by this absorption energy, this specific RF excitation is called as 90° pulse.

After the transmitter is switched off, the protons start remission of the energy at the same frequency ω_0 while the protons realign themselves with the main field. If there is a coil perpendicular to the transverse plane, then there will be an induced voltage in the coil, or the NMR signal which is known as *free induction decay* (FID). The decay of FID is proportional to the re-emission of the absorbed energy of the protons. This re-emission process is referred as the relaxation process of the protons.

2.1.3. Relaxation Mechanisms

After an RF pulse performed to the spin system, the net magnetization of the system, $\mathbf{M}$ will precess around the main magnetic field $\mathbf{B}_0$. During the proton's re-emission of the absorbed energy, there is an RF pulse detected on the coil at the same frequency of the performed pulse, this whole picture of re-emission and detection processes is known as relaxation mechanism. The detected pulse on the coil acts a sinusoidal oscillation which dampens eventually in time with the effect of two relaxation mechanism: *longitudinal* relaxation and *transverse* relaxation.

Longitudinal relaxation, is responsible for the loss of the signal, is also known as the *spin-lattice relaxation*. This mechanism is connected to the z component of the net magnetization ($\mathbf{M_z}$) which regains its equilibrium value $M_{z,eq}$. Consider a transmitter sending an α pulse ($\alpha \neq \pi$) is switched at $t = 0$. Then the longitudinal magnetization holds the equation

$$M_z(t) = M_0(1 - e^{-\frac{t}{T_1}}) + M_z(0^+)e^{-\frac{t}{T_1}}, \tag{2.23}$$

where T_1 refers to the longitudinal relaxation time and $M_z(0^+)$ implies the longitudinal magnetization right after the application the pulse which is defined as

$$M_z(0^+) = M_0 \cos \alpha. \tag{2.24}$$

To reach the equilibrium T_1 relaxation has a direct on the redistribution of the nuclear spins. The relaxation of α pulse negligible compared to T_1 relaxation at NMR frequencies. Since the duration of the emission takes much longer time.

The second mechanism that has an impact on damping signal is the *transverse relaxation* or *spin-spin relaxation*. The transverse relaxation mechanism can be considered as the first reason for the signal to decay. The perturbations of the spins in the main magnetic field induce this relaxation type. This interaction leads spins to speed up or speed down for a moment so that spins acquire different phase compared to other spins. This *dephasing* process strikes the RF pulse emitted by the spins which result in a signal loss in the coil which is defined earlier as FID. The decay in the FID can be represented as an exponential decay whose time constant is known as the *transverse relaxation time*, denoted by T_2 and has units of time. The mathematical expression for this phenomena is given by

$$M_{xy}(t) = M_0 \sin \alpha e^{-i\omega_0 t} e^{-\frac{t}{T_2}} \tag{2.25}$$

T_2 is a significant material property that varies from one tissue to another, providing delicate contrast in MR images. Furthermore, the signal received by the antenna or coil decays more quickly than T_2 in reality. This rapid exponential decay, is indicated by T_2^*, is the consequence of the local perturbations of the main magnetic field B_0. The relation with these two relaxations regarding the perturbative effect of the static magnetic field mechanism can be expressed as

$$\frac{1}{T_2^*} = \frac{1}{T_2} + \frac{1}{T_2^p} = \frac{1}{T_2} + \gamma \delta B_0 \tag{2.26}$$

where γ is the gyromagnetic ratio and δB_0 represents the local variation on the magnetic field. Conversely to T_2, the local irregularities on the magnetic field affects the T_2^* relaxation. Thus, it is always shorter than T_2 relaxation time.

The general Bloch equation which gives the complete picture of relaxation behavior of a magnetic spin system is given by

$$\frac{\mathrm{d}\mathbf{M}(t)}{\mathrm{d}t} = \gamma \mathbf{M}(t) \times \mathbf{B}(t) - R\mathbf{M}(t) - \mathbf{M}_0 \tag{2.27}$$

where R is the *relaxation matrix*, written by

$$R = \begin{pmatrix} \frac{1}{T_2} & 0 & 0 \\ 0 & \frac{1}{T_2} & 0 \\ 0 & 0 & \frac{1}{T_1} \end{pmatrix} \tag{2.28}$$

and $\mathbf{B}(t)$ is the total magnetic, the sum of the static field and RF field,

$$\mathbf{B}(t) = \mathbf{B}_0 + \mathbf{B}_1(t). \tag{2.29}$$

This whole picture depicts the magnetization behavior, and from this, the NMR signal can be deduced by measuring the transverse magnetization.

2.1.4. Imaging Contrast Mechanisms

It is now very obvious that the transverse magnetization $M_{xy}(t)$ generates the MR signal so that the larger magnetization magnitude results in, the larger the measured signal. Due to the intrinsic NMR properties of tissues, the measured signal may vary in tissues. This difference in signal appears itself in the acquired image having different contrast at different tissue region; for example, gray matter (GM) and white matter (WM) of the brain differ at image intensities. In MRI, the tissue contrast can be acquired with both the intrinsic NMR properties of the tissue (that is proton density PD, T1, and T2 relaxations) and the attributes of the applied excitations(i.e., the pulse

sequence). To that extent, we have learned that the RF excitation can be governed by adjusting both the tip angle α and the echo time T_E. The interval between sequential α pulses, known as the pulse repetition interval T_R, can also be controlled. In this part, we will discuss that the response of the small volumes consisting different tissues to the same applied RF excitations and how tissue contrast can be schemed by external user parameters.

2.1.4.1. $\mathbf{P_D}$-Weighted Contrast. P_D weighted image contrast proposes that the image intensity must be proportional to the number of hydrogen nuclei in the tissue. The higher proton number in a tissue leads to a greater transverse component of the magnetization which results in a more brighter signal on the P_D weighted contrast image. A P_D weighted contrast can be obtained by minimizing the effects of T_1 and T_2 relaxation time differences. To diminish the impacts of T_1 and T_2 time constants, a long T_R keeping the tissues in equilibrium and a short T_E minimizing the decay of T_2 can be utilized. Applying a 90° RF pulse allows us to obtain a maximum signal from the tissue.

2.1.4.2. $\mathbf{T_1}$- Weighted Contrast. The T_1 relaxation time is the time that is required for the recovering of the excited spins and is available for the next excitation. Let us consider an example of fat and cerebrospinal fluid (CSF) in the human body to illustrate this mechanism. The statement that the frequency of the hydrogen atoms in CSF is higher than those in fat is consistent with the Larmor equation. From this statement, it is seen that the hydrogen atoms in fat recover more rapidly along the longitudinal axis compared to CSF. The spins of the hydrogen atoms in fat realign themselves with the main static field $\mathbf{B}_0$ faster than those spins in CSF due to the shorter T_1 time of fat. Hence, the longitudinal component of the magnetization of fat is larger than that of CSF.

The next RF excitation is performed after a certain T_R, and then, this new excitation realigns the longitudinal magnetization of fat and CSF with the transverse plane. Conversely to CSF, The longitudinal magnetization of fat can be flipped into

transverse plane more easily due to the more longitudinal magnetization of fat before the pulse. Therefore, it can be deduced that the contribution to the overall signal coming from CSF will be too small compared to fat. That results in more brighter fat tissues than CSF on the image. This is defined as T_1 weighted imaging contrast.

Repetition time T_R has a crucial impact on T_1 imaging contrast. It manages how far each spin recovers itself before applying a next RF pulse to them. T_1 weighted image contrast requires the T_R to be sufficiently short thereby, both fat and CSF have sufficient time to align with $\mathbf{B}_0$ completely. Otherwise, the difference in T_1 contrast can not be seen on the image.

2.1.4.3. **$\mathbf{T_2}$**-Weighted Contrast. As we discussed earlier, the T_2 relaxation time is referred as how quickly an MR signal decays after excitation. Let us continue with the example of fat and CSF. Decay in T_2 arises from the energy transfer between spins. This energy transaction between hydrogen atoms occurs more efficiently in fat in comparison to water. Consequently, hydrogen atoms in fat lose transverse magnetization more rapidly compared to that in CSF. The T_2 relaxation time of fat is shorter than the T_2 time of CSF. Hence, the transverse magnetization of fat decays more quickly. In comparison to fat, CSF contains much more transverse magnetization so that it is illustrated as very bright in T_2 contrast image.

Echo time (T_E) is defined as the interval between application of the RF pulse and measuring of the MR signal. Performing short T_E develops small signal differences between tissues since T_2 relaxation has started shortly before and there has been only little signal decay at the collection of echo time. Hence, the acquired image has low T_2 weighting. Conversely, using a long T_E makes the signal differences large between tissues. The signals of the tissues having short T_2 have decayed much more, and those tissues appear dark on the resulting image whereas the tissues having long T_2 generates a stronger signal so that they appear bright. This explains the brightness of CSF having longer T2 on T2-weighted contrast images in comparison to fat.

2.1.4.4. Inversion Recovery. We have showed that tissues with different T_1 values can be manipulated to obtain different signal intensities by adjusting the T_R of a pulse sequence. Applying an *inversion pulse* at the beginning of a pulse sequence, is that applying a 180° RF pulse, conceptually facilitates establishing T_1 contrast. Conversely to the previous use of a 180° RF pulse for the manipulation of the transverse magnetization, it is performed for the manipulation of the longitudinal magnetization.

Let us introduce a system in equilibrium. Application of 180° RF pulse reverses the longitudinal magnetization and the transverse magnetization becomes zero after this application. The relaxation of tissues with different T_1 values occurs at different rates. An application of imaging pulse during the relaxation after the inversion pulse can capture these different rates.

We have defined earlier that the duration is required for the longitudinal magnetization of a tissue with T_1 relaxation time to become zero is referred as the *inversion time*, T_I. If a 90° RF pulse is applied at this inversion time T_I, the tissue will not have a transverse relaxation, since the transverse magnetization this tissue is equal to zero at $t = T_I$. Hence ,there will be no signal generated at that time. However, other tissues having different T_1 values will continue to contribute to the FID and their contrast, because of non-zero transverse magnetization of them. A spin echo is widely used in inversion recovery because the effects of T_2^* will trigger dephasing of the transverse magnetization by the inversion time T_I, leaving no signal without the spin echo.

The process of inversion recovery can be performed to measure T_1 value of a given tissue by repeating the process with different T_I's. Another important use of inversion recovery experiment is to null out particular tissues including fat (known as *short tau inversion recovery* (STIR) sequences) and fluid (known as *fluid attenuation inversion recovery*(FLAIR) sequences), When one of these tissues is nulled, then the other tissues will have a very high contrast compared to the nulled tissue. This contrast difference can be used to discriminate tissue differences in certain diseases.

2.1.5. Spin Echoes

Pure transverse relaxation, identified by the T_2 relaxation time, is a stochastic phenomenon. In fact, the rapid decaying of the FID with T2* relaxation time is the result of the fixed perturbations in the magnetic field which induces an increase in speed of some precessions and other to slow down, as shown in the top row of the figure (2.3). This dephasing process is discussed in the previous section. These fast spins or lazy spins, guiding or lagging the spin system, can switch roles by applying a short-duration 180° RF pulse so that the fast spins cause lagging and the lazy ones lead the spin system. This whole picture of changing roles of the spins represents the spin echo phenomenon. Formation of a spin echo is a consequence of this new phase position of the spins in which the fast spins catch up and the slow spins relapse, as depicted in the bottom row of the figure (2.3). Accordingly, a spin echo is the signal that is originated by the transverse spins restoring their coherence due to a deliberate 180° RF pulse, after a loss of coherence caused by the transverse relaxation processes. The duration from the initial 90° RF pulse to the generation of the spin echo is called as the echo time, denoted by T_E, and can be adjusted by determining the application time of the 180° RF pulse at $T_E/2$.

Furthermore, there exist two factor that incorporates in causing a decrease in amplitude of spin echoes over time. Foremost, longitudinal relaxation induces a decrease in the magnitude of the transverse magnetization due to the elapsing time during the process of spin echo. This concept is portrayed in the figure (2.3), where the transverse magnetization vector is illustrated as getting smaller with time. The second mechanism is that the coherent echo phase never aligns perfectly because of the stochastic effects of transverse relaxation, as demonstrated in the figure (2.3-f). The first effect may be ignored, since T_2 relaxation time is much shorter than the T_1 relaxation time. Hence, the amplitude of a spin echo can be measured by the ideal T_2 exponential decay of the tissue at $t = T_E$. This statement implies that multiple echoes can be revoked by employing 180° RF pulse and the signal strength of these echoes will decay exponentially with T_2 relaxation time until they vanish at approximately $3T_2$.

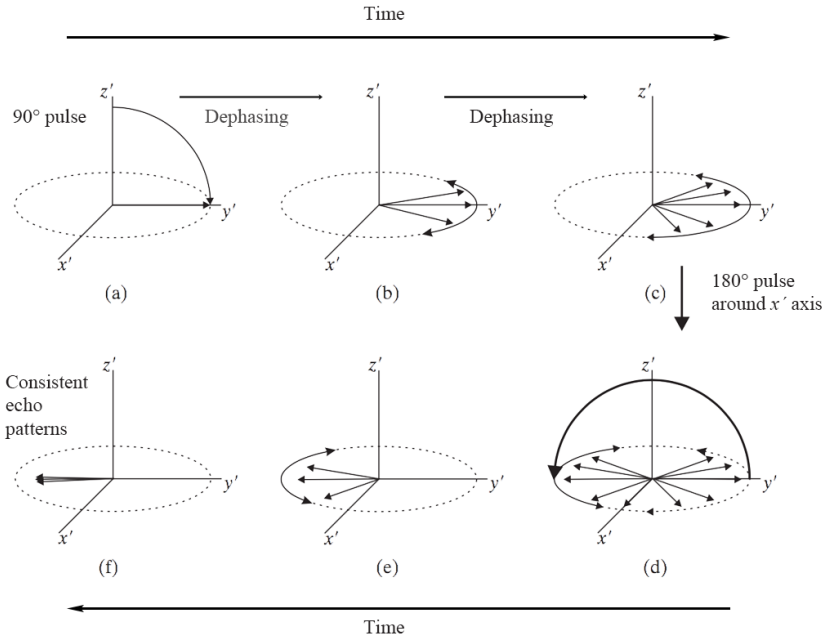

Figure 2.3. The formation of a spin echo

2.1.6. Pulse Sequences

A pulse sequence can be described as the measurement technique for reconstruction MR image. It consists of a user-defined set of RF and gradient pulses and timings that are required to obtain a desired image data. Pulse sequences are usually repeated several times during a scan wherein the time interval between pulses and the amplitude and form of the gradients will govern the acquisition of NMR signal and influence the characteristics of the MR images. Pulse sequences are basically computer programs conducting all hardware features of the MRI measurement process. In this chapter we will describe several pulse sequences commonly used in imaging processes and give a brief instruction about the characteristics of them.

2.1.6.1. Spin Echo Sequences. The spin echo sequence is the most common pulse sequence in MR imaging. It requires at least two RF pulses that are an excitation pulse (α pulse) and one or more 180° recovering pulse that forms the spin echo. The details of the spin echo has been discussed in previous section. Thus, we will continue with the types of spin echo sequences.

Spin echo sequences that utilized mostly divide into three segments: single echo, multi echo and echo train spin echo (ETSE). Standard single echo sequence is mainly used to generate T_1-weighted images. A form of multi-slice loop is utilized with a single pair of excitation and recovering pulses performed within the slice loop. A single phase encoding gradient amplitude (G_{PE}) is applied per excitation pulse. Each spin echo is measured at specified T_E after the application of a different G_{PE}. Then, a rectilinear, sequential filling of k-space is utilized. After image reconstruction, the variations of amplitude between tissues in the image are the consequence of different intrinsic tissue properties (P_D, T_1, or T_2).

In multi-echo sequences, a series of 180° recovering RF pulses are applied after an excitation RF pulse. The spin echoes are generated at a particular T_E by each recovering RF pulse. As in the spin echo sequence, A single G_{PE} is applied per RF excitation pulse. The variations in the G_{PE} still causes the differences in the signal intensity of raw data at each T_E. This procedure introduces the variations from echo to echo in the signal intensity of raw data due to the T_2 relaxation. The signals extracted at each T_E generates the images. Multi-echo sequences performed to acquire P_D-weighted images using short T_E ($< 30\,ms$) and T_2-weighted images using long T_E ($> 80\,ms$) when T_R is sufficiently long to permit relatively complete T_1 relaxation for most tissues ($2000\,ms$ or greater).

Lastly, the third type of spin echo sequence is referred as the echo train spin echo (ETSE) relying on the rapid acquisition and rapid enhancement (RARE) imaging technique. ETSE resembles the multi-echo sequences through performing multiple 180° pulses to generate multiple echoes after an excitation RF pulse. Although, each echo signal is generated by a different G_{PE} and T_E. The image is created by utilizing some or all of the acquired echoes as determined by the sequence profile. The echo train length represents the number of echoes used to generate image. In this sequence type, a segmented filling of k-space is utilized with one echo to from each segment obtained as the echo train part for each RF pulse. The fundamental benefit of the ETSE is that the process of data collection is more efficient and the time for scanning is reduced.

2.1.6.2. Gradient Echo Sequences. Conversely to the spin echo, In gradient echo sequences, a 180° RF pulse is not performed to recover the spins. An application of gradient pulse induces dephasing of the spins. To refocus these spins, the opposite polar of the prior gradient pulse is applied to reverse this dephasing of the spins and generates the gradient echo. All gradient echo sequences requires gradient reversal pulse in at least two directions, the slice selection and the readout directions, which produce the echo signal.

In gradient spin echo sequences, due to the absence of the 180° RF pulse, the kernel time of the sequence might be shorter than for a correspondent spin echo sequence. This reduction of time enables a shorter minimum T_R or acquisition of more slices for the same T_R in a multi-slice loop. Moreover, another consequence of the absence of 180° RF pulse is that the RF power applied to the patients is less so that the RF energy accumulation in the body is lower. In addition to contrast mechanism, the inhomogeneity of applied field $\mathbf{B}_0$ and the magnetic susceptibility, that trigger the dephasing of protons, play a part in signal decaying. Thus, the T_E determines the T_2^* weighted image in gradient echo sequence rather than the T_2 weighted image in spin echo sequence. Therefore, the overall level of the signal in gradient echo sequences is less in comparison to that in spin echo images with comparable parameters.

2.1.6.3. Echo Planar Imaging Sequences. In an echo planar imaging (EPI) sequence, a unique method is employed for data collection. Applying a series of reverse gradient waveforms in the readout direction forms the EPI sequences. These inverted gradient waveforms generate a gradient echo, with the second half a readout period being rephased by the first half of the following readout period. Swift application of these reversing gradients enables constructing EP images in $100 - 200\,ms$. Thus, the EPI sequences are very responsive to the effects of T_2^* relaxation. Particularly, the differences in magnetic susceptibility cause distortion effects on the image of tissue interfaces (i.e., tissue-bone or tissue-air). These image distortions make the use of tissue interfaces problematic in some anatomical regions.

There are two types of data collection methods are performed in EPI sequences. The first one is the single-shot technique, acquiring all phase encoding steps after a single excitation RF pulse. Due to the one-time application of the RF pulse per slice position, each image can be obtained with an infinite like long T_R. Single-shot EPI method might necessitate modern gradient amplifiers acquire all the echoes, due to the quick switching of the readout gradient polarity necessary to obtain all the echoes. In multi-shot or segmented EPI technique, after each excitation RF pulse, a subset of phase encoding steps can be acquired. A segmented loop system with multiple excitation RF pulses is employed to obtain all phase encoding steps. In segmented EPI method, an older imaging gradient can be used for acquiring all phase encoding steps.

2.1.6.4. Inversion Recovery Sequences. Inversion recovery (IR) is a kind of a spin echo sequence, including an additional 180° RF pulse. An IR sequence is often used for slice selection purpose and performed before the initial excitation RF pulse. The additional 180° RF pulse inverts the magnetization $\mathbf{M}$ of the spins within a given slice, providing augmented T_1 sensitivity at the time of the excitation RF pulse. The inversion time, denoted by (T_I), is an adjustable delay time between the 180° RF pulse and the excitation RF pulse and adjust the amount of T_1 relaxation occurring in this interval. A standard gradient waveforms are used, and the echo time T_E is modified as for in spin echo sequences. To have a maximum T_1 relaxation between sequential excitation RF pulses, IR sequences require long repetition time T_R. Short T_R times trigger signal loss because of the saturation for tissues with long T_1 times.

IR pulses are compatible with all the pulse sequences mentioned, thereby it can be employed with them. IR sequences are frequently used with the ETSE sequences; however, their applications with EPI sequences are also common to some extent. The echo train inversion recovery sequence connects the IR features with the ETSE sequences. The 180° RF pulse is performed before an ETSE sequence instead of a standard spin echo sequence. The inversion time T_I and the tissue T_1 relaxation times as in the IR sequences forms a basis on the acquired contrast in an echo train IR sequence, whereas the length of the echo train and effective T_E have similar impacts on these parameters

in the ETSE sequence. The following alteration is the looping procedure for multi-slice imaging. In a case of sufficiently short T_I times, all RF pulses are performed, and the signal is measured from a slice before advancing to the next slice. In the opposite case, all inversion RF pulses are performed respectively, pursued by the excitation and recovering RF pulses and signal detection. As a consequent of this, in a T_R period, a more efficient process of data collection will be provided.

2.2. Principles of Image Acquisition in MR - PART I

In previous sections, the behavior of a nucleus experiencing an external magnetic field is discussed that cause a precessing at a particular frequency. Throughout this precessing, MRI utilizes the field dependence of the protons that absorbs the frequency of energy to localize them to different regions. In MRI, employing the magnetic field gradients makes the main magnetic field spatially dependent. Then, the net magnetic field is experienced by the tissue is given by

$$\mathbf{B}(t) = (B_0 + \mathbf{G}(t) \cdot \mathbf{r}(t))\hat{\mathbf{r}} \tag{2.30}$$

where $\mathbf{G}(t)$ represents the magnetic field gradient vector ($\mathbf{G}(t) = (G_x(t), G_y(t), G_z(t))$ and $\mathbf{r}$ is the position vector for the corresponding region and has units of milliTesla per meter $\frac{mT}{m}$. The gradient fields, in MRI, compose linear variations in one direction, three physical x, y, and z directions. Through these physical directions, MRI can be *tomographic* meaning that it enables us to choose specific slices of the body for selective imaging. Moreover, gradient fields promises spatially encoding the picture elements (pixels) within a selected image slice as a consequence of that each FID and echo stemming from each pixel within the slice can be untied and transformed to an image.

With the enhancement of the magnetic field by introducing the gradient field, the Larmor equation (2.6) yields

$$\omega = \gamma(B_0 + \mathbf{G}.\mathbf{r}) \tag{2.31}$$

where ω represents the net frequency of the proton at position $\mathbf{r}$. Hence, the Larmor frequency becomes position dependent so that each proton will precess at a unique frequency in the gradient field. The MR image is generated by a frequency and phase map of the protons emerged by different magnetic fields at each point everywhere in the image. The displayed images involve pixels substituting for volume elements (voxels) of tissue. The intensity of the pixel is correlated with the proton number in the voxel.

To construct NMR images there exist certain procedures that must be followed. To generate MR image data, the region of interest must be well defined through slice selection procedure. Then, frequency and phase encoding systems are required to extract the NMR signal and imaging it. These three procedures can be considered as the fundamental pillars of the NMR image reconstructing.

2.2.1. Slice Selection

To generate images in NMR, it is crucial to define the area of interest, is the localized RF excitation into the corresponding region, can be fulfilled by utilizing the frequency-selective excitation conjugated with a gradient field referred as slice selective gradient, indicated by $\mathbf{G}_{SS}$. The slice orientation is determined by the gradient direction (x, y, or z). Meanwhile, in determining the slice thickness and slice position, the amplitude of the gradient field together with a certain type of RF pulse are assigned. A frequency-selective RF pulse consists of two main elements: a central frequency and a narrow range of frequencies (varying 1-2 kHz). While the slice selection gradient field is applied, if a frequency-selective pulse is transmitted, the protons in a narrow regime absorb the resonant frequency of energy (Equation 2.31). The amplitude and the duration of the RF pulse settle the amount of rotation that associated protons make (for instance, 90° or 180°). The second element, the central frequency of the pulse, regulates

the particular region excited by the pulse in the presence of the gradient field. Changing the value of the central frequency adjusts the slice position. Obtaining different slice thicknesses can be achieved by modifying the gradient amplitude and the range of frequencies of the RF pulse. The thinner slices require larger gradient amplitude $\mathbf{G}_{SS}$. Once the slice thickness is determined, the central frequency is computed to resonate the protons in the desired region. Multi-slice imaging is a widely used approach in MRI that utilizes the same $\mathbf{G}_{SS}$, however, during the excitation, it uses a unique RF pulse for each slice. As a result of this difference, different regions of the tissue is excited by the same RF pulse with a different central frequency.

The orientation of the slice is specified by the physical gradient or gradients introduced as the slice selection gradient. The gradient orientation is set perpendicular to the surface of the slice, thus all protons within the slab experience the same magnetic field despite their position within the slice.

2.2.2. Frequency Encoding

The frequency measurement or readout is responsible for the signal detection in MRI measurement. This process separates MRI from MR spectroscopy, another type of MR process. The gradient field referred as the *readout gradient* ($\mathbf{G}_{RO}$) is employed to detect the MR signal in an imaging pulse sequence. The readout gradient generates a visual dimension of the 2D image. An ordinary pulse sequence employs some profile of excitation, such as a 90° slice-selective pulse, to stimulate a particular tissue region. After excitation, the net magnetization of the protons within the slice is adjusted transverse to the main magnetic field $\mathbf{B}_0$ and will start precession at frequency ω_0. T_2^* relaxations cause dephasing of this transverse magnetization, discussed previously. Applying a 180° RF pulse, a gradient pulse or both partially invert this dephasing process to produce an echo. When the echo is formed, the readout gradient is employed perpendicular to the direction of the slice. According to the equation (2.31), the protons experiencing the new gradient field start precessing at different frequencies based on their positions in this gradient field. Each of these different frequencies is laid into the echo. Thereby, at any time, the echo signal is measured by the receiver antenna and

digitized for Fourier transformation. The measured frequency and the magnitude of the readout gradient $\mathbf{G}_{RO}$ allow the associated proton position to be specified.

In an NMR image, the two aspects of defining the resolution are spatial resolution and frequency resolution. The spatial resolution, can be introduced as the voxel size having units of millimeters per pixel ($\frac{mm}{pixel}$), is measured by the parameters adjusted by a physician that are the field-of-view in the readout direction, and the sample points of readout in the acquisition matrix. The frequency resolution, having units of hertz per pixel ($\frac{Hz}{pixel}$), depends on also the number of readout sample points in the acquisition matrix and the total range of frequencies in the image.

Improving the frequency resolution for the measurement regardless the spatial resolution can be achieved through increasing the total sampling time employed in measuring the signal. Increasing the sampling time does not result in requiring more time since the frequency encoding is concerned with how rapidly the FID signal is sampled by the scanner.

2.2.3. Phase Encoding

The phase encoding direction constitutes the third direction of an MR image that is pictured along with the readout direction. The phase encoding gradient ($\mathbf{G}_{PE}$), is perpendicular to the both $\mathbf{G}_{SS}$ and $\mathbf{G}_{RO}$, changes amplitude during the data collection cycle of a standard 2D imaging sequence. Since G_{PE} the only gradient that varies amplitude in this imaging process, any detected variation on the signal from one acquisition to another can be considered as the impact of $\mathbf{G}_{PE}$ during the measurement.

The fact of the periodic proton precession constitutes the principle of the phase encoding. Before the application of $\mathbf{G}_{PE}$, protons in a tissue precess at the base frequency ω_0. Employing $\mathbf{G}_{PE}$ increases or decreases the frequency of these proton precessions according to equation (2.31). When the application of $\mathbf{G}_{PE}$ is ceased, the precession of the protons recovers their base frequency while, in phase, these precessions remain ahead or behind compared to their previous state. The magnitude and

application duration of $\mathbf{G}_{PE}$ experienced by the protons and the position of the protons determine the amount of accumulated phase shift. Protons at different positions acquire different amounts of phase shift for the same $\mathbf{G}_{PE}$ pulse in the phase encoding direction. In addition to that, a proton placed at the edge of a given FOV gains the maximum amount of phase shift from each phase encoding process. Repeating the slice excitation and signal measurement several times, each with different $\mathbf{G}_{PE}$ amplitude generates the MR image data. The signal amplitude at each readout frequency is transformed from a G_{PE} function to a phase function by performing the second Fourier transformation in the image.

The spatial resolution in the phase encoding direction is defined as the voxel size and has the units of millimeter per pixel ($\frac{mm}{pixel}$) which can be adjusted by two user parameters that are the field-of-view (FOV) in this direction and the number of phase encoding steps in the acquisition matrix. To increase resolution in an image one needs to adjust these two parameters by reducing the FOV in the phase encoding direction or increasing the number of phase encoding steps in the acquisition matrix. The reduction of FOV is proportional to an increase in the amplitude of the gradient G_{PE}. Since the variation in G_{PE} from one process to next one determines the FOV in the phase encoding direction.

The FOV or the voxel size in phase encoding direction and is not necessarily the same as the FOV or the voxel in readout direction because of participation of two distinct physical parameters, respectively. The ratio of the voxel size in readout direction to the voxel size in phase encoding direction expresses the aspect ratio between this two dimensions. An aspect ratio of 1.0 yields a case referred to as isotropic resolution implying that the voxel size in both directions is the same. When this ratio is less than 1.0, anisotropic resolution case arises and the voxel size in the phase encoding direction is larger than that in readout direction.

2.3. Principles of Image Acquisition in MR - PART 2

In previous sections, we have described the fundamental steps for spatial localization of the MR signal. For complete comprehension of MRI, one needs to be presented some additional concepts that illustrates the full picture of MRI. In this section, the concepts that we are going to discuss may be considered with any MRI measurement technique that we have studied so far.

2.3.1. Frequency Selective Excitation

The RF pulses contain a number of complex data points with amplitudes and time varying phases. The digital points of a RF pulse are converted to analog format before combining with the base frequency and amplification. The RF waveforms are determined by diverse parameters that might be adjustable or predefined depending on the software of the manufacturer.

It would be great to have a brief description about the two main type of pulse shapes: Non-selective pulses and selective pulses.

- Non-selective pulses have constant amplitude and short duration. They excite a wide range of frequency with a uniform amplitude. The rectangular pulses can be given as an example to the "non-selective" pulses. Despite of their name, they are frequency selective because the frequency range, that can be merged with the pulse is restricted by the pulsed nature of the excitation shown in the figure (2.4).
- Selective pulses have varying amplitudes during broadcasting and longer pulse durations, limiting the frequency range. There are three types of selective pulses that are used frequently. The sinc pulses and Gaussian pulses illustrated in the figures (2.5,2.6) are the example of the selective pulses that are primarily utilized.

There are some criteria that bind the RF excitation pulse. Firstly, to achieve the same flip angle, short duration pulses are in need of high peak pulse amplitudes. The max power of transmitted pulse depends on the RF amplifier and transmitter. The next

issue is that while the amplitude of the pulse is increased, the stored power in the pulse increases as quadratically. Thus, longer pulse durations are required to diminish the stored power of the pulse, which may lead an increase in T_R and T_E. Furthermore, the sinc functions at low flip angles ($< 30°$) generate rectangular excitation forms that are inconsistent with phase. Conversely to that, non-rectangular excitation profiles are produced by the high amplitude sing pulses such as 90° and 180°. The last criterion is that there is an inverse proportional relationship between the RF pulse duration and the frequency range of the pulse so that as the duration increases, the bandwidth decreases. This means that to focus the energy to the same tissue region, less slice selection gradient G_{SS} is needed. Nevertheless, the sharpness of the slice form is also reduced when the slice selection gradient G_{SS} is reduced. This can trigger well-defined crosstalk between slices or sensitivity to the diversity of magnetic susceptibility within the slice, generating nonuniform image intensities, specifically at ultra-high field strengths.

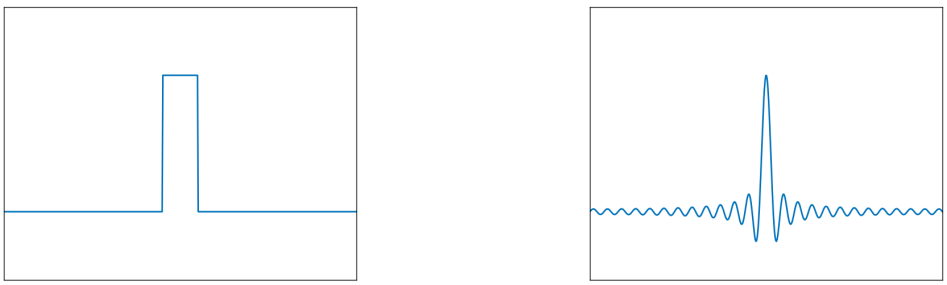

(a) Time domain (b) Frequency domain

Figure 2.4. Rectangular (Non-selective) RF pulse waveforms

(a) Time domain (b) Frequency domain

Figure 2.5. Truncated Sinc (Selective) RF pulse waveforms

(a) Time domain (b) Frequency domain

Figure 2.6. Gaussian (Selective) RF pulse waveforms

2.3.2. Raw Data and Image Data Matrices

In measured MRI data analysis, the acquired data can be considered in two different formats that are the raw data and image data. Even though, each data set comprises the same information obtained from the slice or slices. The application purpose is different for both data sets. They are collected and configured as a matrix of points characterizing the slice. The raw data format is generated in the process of data collection and utilized in that process. On the other hand, the image data format is generally utilized for viewing and interpretation. Consequently, both data sets are related to Fourier transformation.

In MRI, the raw data arises from the digitized information measured for a certain echo from a given slice. The amplitude of the echo signal is digitized as a function of

time, whether an analog or digital receiver is employed. The digital signal form is stored as a data array rendering real and imaginary values. Each row of the matrix of raw data, representing the measured amplitude of the signal for a particular echo, varies depending on the value of the phase encoding gradient G_{PE}. The rows are ordered from top to bottom as an increasing fashion of the phase encoding amplitudes. Thereby, the raw data matrix can be considered as a grid of points in which the readout direction is displayed horizontally, and phase encoding direction is displayed vertically. Hence, both the number of readout data points and the number of phase encoding steps determine the dimensions of the raw data matrix.

The matrix of image data format is constructed by the 2D Fourier transformation of the raw data matrix. The image matrix consists of a complicated frequency and phase map of the signal intensity of protons in a region that is weighted by the T_1 and T_2 values of the tissues within the region. These frequencies and phases are spatially dependent according to the location of the region, and the base transmitter frequency determines the measurement of these frequencies and phases. The image matrix is formed by an array of values representing either the relative phases or the signal magnitudes. Image matrix is displayed as square arrays consisting phase encoding as one direction and readout as the other direction in the image; even it has to be the same dimension as the raw data matrix. This can be achieved by employing interpolation process that is performing Fourier transformation to create more image pixels originating from the initial pixels. The determination of the rows and columns as the readout or phase encoding depends on the choice of operator and in general, it is set in a manner minimizing the artifacts.

2.3.3. Signal to Noise Ratio

The signal to noise ration (SNR) of MRI data, which is one of the key features of both the raw data and image data, is subject to both the signal level and the noise level existing in the data. Various factors influence the signal level and the noise level. For instance, the size of a volume within a voxel is proportional to the signal. Also, When the sampling time increases, the noise level decreases, causing a rise in

SNR. Furthermore, the features of the MRI hardware such as the strength of the main magnetic field, the volume of the receive coil and the sensitivity of the receive coil. Finally, tissue relaxation and other properties may contribute to the signal which have an impact on the SNR. Consequently, in order to improve SNR, a decrease in either spatial resolution or sampling time must be encountered. Otherwise, to have a better resolution, either a decrease in the SNR is required or the sampling time must be increased.

2.3.4. Raw Data and k-Space

The raw data matrix, an important structure in MRI, represents each slice in a given volume before processing the data and also contains all the information required to construct an image. All the points within the raw data matrix promote to all characteristics (frequency, phase, and amplitude) of every location inside the slice.The higher signal data are stored in the center region of the raw data matrix. The outer parts of the raw data matrix consist of relatively low signal content and are obtained with the absolute high G_{PE} amplitudes. These gradients yield high frequency (according to the Larmor equation) and ensure primarily edge definition to the image.

The k-space formalism, an alternative approach describing the raw data matrix, provide a convenient description of the procedures for obtaining raw data. In this methodology, the complex array of the raw data points is depicted as a two-dimensional grid of points, that are k_x representing a point in the readout direction of the raw data and k_y representing a point in the phase encoding direction. Each pair of (k_x, k_y) data point expresses the amplitude of echo signal effected by the combination of readout and phase encoding gradient moments:

$$\begin{aligned} k_x &= \gamma G_{RO} t_{RO} \\ k_y &= \gamma G_{PE} t_{PE} \end{aligned} \tag{2.32}$$

where t_{RO} and t_{PE} represents the total application time of gradient pulses. This equation states that at each point of (k_x, k_y) the total impact the of gradient is different and unique. The origin of k-space $(0, 0)$ has the maximum amplitude in the raw data matrix. Th k-values have the units of an inverse millimeter $(\frac{1}{mm})$ corresponding the spatial frequencies. In k-space formalism, the image contrast is subject to the relatively low spatial frequency data surrounding the center, whereas edge definition depends on the high spatial frequency data at the edges of k-space.

In 3D scanning procedures, to complete 3D format, k-space formalism utilize another direction, k_z corresponding to the gradient pulse in the slice selection direction:

$$k_Z = \gamma G_{SS} t_{SS} \tag{2.33}$$

where t_{SS} is the total time that the slice selection gradient G_{SS} is applied. The same principles for the k-space of 2D images are also valid for the 3D imaging process. In 3D images, the raw data become a 3D volume defined by (k_x, k_y, k_z) similar to the 2D data representation mentioned earlier. The image contrast is promoted mostly by the origin of the k-space $(0, 0, 0)$, while the edge definition in the final image is promoted by the edges of the k-space.

Continuous sampling of the raw data space and employing a uniform density in a given direction result in producing images without artifacts. In other words, the change in k-space, Δx and Δy, must be constant and span the entire space. However, they do not require to be equal. By this requirement, the equal weighting on both contrast and edge definition in the image is ensured. To execute these demands, there is an approach, referred as the rectilinear data collection method can be performed.

2.3.5. k-space Filling Techniques

Before initiating Fourier transformation process, a uniform k-space density is required; yet, the order of acquiring the each k_y line is a random procedure. This order of filling represents the well-known k-space trajectory. The most common procedure

for data collection is a linear trajectory. The raw data matrix is filled with one k_y line that is acquired successively in time, one by one. During application of the readout gradient G_{RO} in a constant period and amplitude, the process of echo sampling with a constant dwell time is performed. Alternative methods for the process of k-space filling is utilized for some special cases where additional contrast manipulation is required. The methods of acquiring the raw data in a nonconsecutive way are known as the reordered k-space filling methods. In centric ordered k-space filling techniques, the lower amplitude G_{PE} steps are acquired earlier than that of higher ones. Acquiring the $k_y = 0$ signal at different times of the scan leads variations on the sequential and centric ordering. These approaches may be effective in some scans where the net magnetization $\mathbf{M}$ can not reach sufficiently the steady-state value in the initially detected echoes. Measuring the $k_y = 0$ signal at immediately after the beginning of the scan will influence $\mathbf{M}$ to have a closer value to the steady-state with the help of the initial RF pulses of the sequence.

Another useful way to collect data is referred as the segmented method, in which the sequential echoes measure lines from the different segments of k-space. The data collection procedure is fulfilled in a segmented-serial way so that one phase encoding step from each segment.

In 3D scans, there are two approaches that the reordering of k-space can be performed. The uncorrelated gradient tables (k_y and k_z) are not necessarily varied in the same way so that one table can be used for sequential ordering method whereas the other is used for centric ordering method. Spiral scanning in 3D scanning is concerned with the stepping ordering of the k_y - k_z gradients whose variations form a spiral. Employing this method in acquiring the echoes determining tissue contrast reduces motion artifacts and allows tissue contrast manipulation.

2.4. Diffusion and Anomalous Diffusion

Diffusion is the net movement of particles or molecules from highly concentrated region to lower concentrated region. Despite its literal meaning, diffusion is governed as a methodology for mathematical modeling implementation of a problem or a simulation in many different disciplines. In this context, diffusion is considered as a spread-out or a stochastic movement of particles from a point or a region rather than its phenomenological meaning.

In the phenomenological aspect, diffusion is the movement of a sample of particles from a highly concentrated region to a lower one without bulk motion effects. The mathematical description of this concept, given by Adolf Fick (1855) [29], is the Fick's law of diffusion. In the physical context, diffusion is depicted as a stochastic movement of diffusing particles [30].

The concept of diffusion was first introduced as a Brownian motion of dust particles in the scientific poem of the Roman Lucretius (On the Nature of Things, 60 BC). After decades, although, Jan Ingenhousz demonstrated a description of the irregular motion of the coal dust on the surface of alcohol in 1785. The Brownian motion was credited to the botanist Robert Brown in 1827 because of his work on the pollen grains completing jittery motion in a fluid.

The mathematical description of Brownian motion is first presented by Thorvald N. Thiele in a paper on the least squares published in 1880. Then, an independent study was conducted by Louis Bachelier in which a stochastic analysis of the stock and option markets was presented in 1900. Due to the discontinuity in the stock price movements, the applicability of Brownian motion in this area was rejected by Benoit Mandelbrot [31].

Einstein [32] and Smoluchowski [33] suggested the solution of the problem regarding physicists, and the equations describing the Brownian motion that they derived was verified by the research of Jean Baptiste Perrin in 1908.

To get a notion of the physical meaning of diffusion many different ways can be demonstrated to describe this phenomenon. A process of diffusing particle performs can be considered as a random walk. Henceforth. we can employ the mathematical model of random walk process on this phenomenon. For simplicity assume a particle diffusing in 1D. For each time δt, it moves δx in coordinate space to the right with probability p_- and to the left with probability p_+, and also stays at the same position with probability $p_0 = (1 - p_- - p_+)$. The general probability of finding the particle in the interval $[x - \delta x, x + \delta x]$ at time $t + \delta t$ is given by

$$p(x, t + \delta t) = p_+ p(x + \delta x, t) + p_- p(x - \delta x, t) + (1 - p_+ - p_-)p(x, t). \tag{2.34}$$

Let us now consider the case that the probability of moving in each direction is equal, *i.e.* $p_+ = p_-$. Then, performing a Taylor series expansion yields

$$\frac{\partial p}{\partial t} = p_+ \frac{(\delta x)^2}{\delta t} \frac{\partial^2 p}{\partial x^2} + \mathcal{O}(\delta t) + \mathcal{O}(\delta x^4). \tag{2.35}$$

From the resultant equation we can deduce the diffusivity or the diffusion coefficient D that is

$$D = p_+ \frac{(\delta x)^2}{\delta t} \tag{2.36}$$

and after a generalization to three dimensional case, the diffusion equation will be derived

$$\frac{\partial p}{\partial t} = D \nabla^2 p \tag{2.37}$$

which was the result of Einstein's study on Brownian particles [32, 34].

The further step would be the mean square displacement computation, to do that let us start with the normalization condition of the probability of a particle being

somewhere at the coordinate space which can be written as

$$\int p(\mathbf{r},t)\mathrm{d}\mathbf{r} = 1. \tag{2.38}$$

The expectation value for a coordinate direction, x, of the particle is defined as

$$\langle x\rangle = \int xp(\mathbf{r},t)\mathrm{d}\mathbf{r}. \tag{2.39}$$

Then, integrating the diffusion equation (2.37) over all space and substituting the expectation value of x into the diffusion equation give

$$\frac{\partial}{\partial t}\langle x\rangle = D\int_{-\infty}^{\infty} x\frac{\partial}{\partial x^2}\left(\int\int p(x,y,z,t)\mathrm{d}y\mathrm{d}z\right) = 0. \tag{2.40}$$

From the above equation, it can be easily deduced that

$$\langle x\rangle = constant. \tag{2.41}$$

Although, the expected position of the particle does not vary, the *variance* of its position depends on time that is determined by

$$\sigma_x = \langle(x-\langle x\rangle)^2\rangle \equiv \langle x^2\rangle - \langle x\rangle^2. \tag{2.42}$$

The next step will be performing the same procedure that we used, injecting the variance equation into diffusion equation, yields

$$\frac{\mathrm{d}\sigma_x}{\mathrm{d}t} = D\int_{-\infty}^{\infty}(\langle x^2\rangle - \langle x\rangle^2)\frac{\partial}{\partial x^2}\left(\int\int p(x,y,z,t)\mathrm{d}y\mathrm{d}z\right) \tag{2.43}$$

After calculating the integral equation above, therefore, we find the famous result of Einstein [34]

$$\sigma_x = 2Dt \tag{2.44}$$

which is the *mean squared displacement* (MSD) of the particle. Notice that the distance traveled by the diffusing particle in time t is proportional to $\sqrt{t}$. In 3D case the MSD would be $\sigma_{\mathbf{r}} = 6Dt$ with the contributions of other directions.

2.4.1. Anomalous Diffusion

As we have already mentioned, a diffusion process is in linear relation with time as Einstein suggested, and this relation is referred to as mean square displacement. In general, however, there exist some diffusive motions that do not obey this relation. The relation of these processes to time can be non-linear conversely to the "normal" diffusion processes. The diffusive processes that have a non-linear relationship with time are referred as the anomalous diffusion processes. Unlike normal diffusion, anomalous diffusion is expressed by a power law [35–40], represented as

$$\langle r^2(t) \rangle = t^a \tag{2.45}$$

where a is a real number. The equation (2.45) is an expression for general diffusive processes that can be categorized through the scaling index a. When $a = 1$ the resultant motion will be the normal diffusive motion. If $a > 1$, the resultant motion becomes super-diffusive motion. Conversely to that, the sub-diffusive motion takes place if $a < 1$.

The anomalous diffusive processes is a delicate phenomenon for modeling the various diffusion scenarios such as particles diffusing in a crowded environment. For instance, inter cellular protein diffusion and the diffusion of the particles through porous media. Sub-diffusion has been offered as a measure of macromolecular crowding in the cytoplasm.

Recently, anomalous diffusion was observed in different research areas including ultra-cold atoms [41, 42], the motion of Telomeres in the cell nucleus [43–45], in single particle movements in cytoplasm [44, 46], and in worm-like micellar solutions [40]. Furthermore, anomalous diffusion was discovered in other biological structures within

heartbeat intervals [47] and DNA sequence [48, 49]. Conversely to that, anomalous diffusion is also a research topic of climatology. The daily fluctuation of temperature is considered to be as a diffusive process and have been observed as anomalous.

There are a variety of frameworks leading anomalous diffusion that are seriously studied as the concept of statistical physics. These are continuous-time random walks (CTRW) [50, 51] and fractional Brownian motion (fBm), long range correlations between the signals [52], diffusion of particles in a 2D bacterial suspension [53], and diffusion in disordered media [38, 54].

2.4.2. Fractional Brownian Motion

A Gaussian normal process is a Brownian particle's stochastic movement so that the mean square displacement of the walker has linear proportionality to the time as in the results of Einstein's theory of Brownian motion [32]. The probability distribution for such process is the Gaussian normal distribution which can be measured in normal diffusion, random walks, Langevin equation, diffusion equation and Weiner processes, and so forth. Conversely to the standard diffusion, there exist processes or motion that not obey the Einstein's theory so that the mean square displacement of such motion scales as a fractional power in time. These processes or motions are referred as continuous-time Gaussian processes, and the most basic example of it is the *fractional Brownian motion* (fBm).

In this section, we study for the mathematical description of anomalous diffusion as a fBm process. To tackle with mathematics behind this phenomena we will introduce some properties for our process and fractional calculus. Now, let us consider a fBm process $x_H(t)$ on the interval $[0, T]$, having the initial condition $x_H(t) = 0$. The expectation value of this process is $\langle x_H(t\rangle) = 0$ and the process has the following covariance function

$$\langle x_H(t)x_H(s)\rangle = \frac{1}{2}[|t|^{2H} + |s|^{2H} - |t-s|^{2H}] \tag{2.46}$$

where H is a real number in the interval $(0, 1)$,which is also known as the Hurst index, Hurst exponent [55], associated with the corresponding fBm. The Hurst index is called as the "index of dependence" which determines the raggedness of the process [56]. As it seen in the equation 2.46, the mean square displacement of the process scales in a fractional manner depending on the value of H. The resultant motion is described by the Hurst exponent as different fBm types;

- if $H = \frac{1}{2}$ the process is a "normal" Brownian motion, or standard diffusion
- if $H > \frac{1}{2}$ the process is referred as a super-diffusive motion as a result of positively correlated increments
- if $H < \frac{1}{2}$ the process is referred as a sub-diffusive motion as a result of negatively correlated increments

where the increment process is a fractional Gaussian noise ($X(t) = x_H(t+1) - x_H(t)$). There exists several properties of the fractional Brownian motion which are explained below.

- Self-similarity: fBm is the only self-similar Gaussian process, which means that in terms of probability distributions, $x_H(at) \sim |a|^H x_H(t)$;
- Stationary increments: the increments $X(t) = x_H(t+1) - x_H(t)$ are known as fractional Gaussian noise and such increments are stationary $x_H(t) - x_H(s) \sim x_H(t-s)$;
- Long-range dependence: when $H > \frac{1}{2}$ the process exhibits long-range dependence as indicated by $\sum_{n=1}^{\infty} \langle x_H(1)(x_H(n+1) - x_H(n))\rangle = \infty$;
- Regularity: sample-paths are almost non-differentiable. However, almost all trajectories are Hölder continuous for any order strictly lower than H. That is, for each trajectory there exists a constant c such that $|x_H(t) - x_H(s) \leq c|t-s|^{H-\kappa}$ for all $\kappa > 0$;
- Dimension: the graph of $x_H(t)$ has both Hausdorff dimension and box dimension $= 2 - H$, with probability 1.

Furthermore, fBm can be generalized to the *n-th order fractional Brownian motion* (n-fBm) which is also a Gaussian, self-similar, non-stationary process of which increments of order n are stationary [57]. The classical fBm can be obtained by setting $n = 1$.

Before starting calculations, let us introduce the well-known Langevin equation in one dimension for Brownian motion,

$$x(t) = x_0 + \int_0^t \upsilon(t')\mathrm{d}t' \tag{2.47}$$

where $\upsilon(t)$ can be considered a Gaussian stochastic speed parameter that has delta correlation $\langle \upsilon(t)\upsilon(s)\rangle = \delta(t-s)$. Using path integral aproach, we want to calculate a general propagator, satisfying all processes depending on the values of H, that measures the probability of finding a Brownian particle at a position x at time t ($t > 0$).This propagator denotes the anomalous diffusion processes and leads to find a general diffusion equation that gives solutions for the corresponding fractional Brownian motion depending on the process. The propagator for the normal Brownian motion is written by

$$\mathcal{G}(x,t|x_0,0) = \frac{1}{\sqrt{4D_0\pi t}} \exp\left(-\frac{(x-x_0)^2}{4D_0 t}\right) \tag{2.48}$$

where D_0 denotes the free diffusion coefficient and for simplicity in notation we will assume $D_0 = \frac{1}{2}$. Then, the diffusion equation satisfying the corresponding propagator is given by

$$\frac{\partial \mathcal{G}(x,t|x_0,0)}{\partial t} = \frac{1}{2}\frac{\partial^2 \mathcal{G}(x,t|x_0,0)}{\partial x^2}. \tag{2.49}$$

There exists various representations in the literature for generalization of Brownian motion, the most convenient way of making this generalization is employing the fractional calculus [58, 59] which was proposed including spatio-temporal correlations

in different approaches [56,60–62]. The algebraic background of the fractional calculus will not be discussed deeply since it just help us integrating or differentiating functions in any order, for example, calculating the α order integration of a function where $\kappa \in (0,1)$. In the Appendix section, a brief review of the fundamental elements about the fractional calculus is provided. The integral operator of order $H+\frac{1}{2}$, is known as the *Riemann-Liouville fractional integral operator* [58,59], is given by

$$ {}_0\mathcal{D}_t^{-(H+\frac{1}{2})}[\upsilon(t)] = \frac{1}{\Gamma(H+\frac{1}{2})}\int_0^t (t-t')^{H-\frac{1}{2}}\,\upsilon(t')\mathrm{d}t' \tag{2.50} $$

substituting this operator into the Langevin equation (2.47) gives us the general representation

$$ x(t) = x_0 + \frac{1}{\Gamma(H+\frac{1}{2})}\int_0^t (t-t')^{H-\frac{1}{2}}\upsilon(t')\mathrm{d}t', \tag{2.51} $$

to simplify the notation we will use the fractional differential operator [60] which is written by

$$ x(t) = x_0 + {}_0\mathcal{D}_t^{-(H+\frac{1}{2})}[\upsilon] \tag{2.52} $$

To calculate the propagator, an approach, was provided by [62], will be used, and the notation in the approach might differ from original one. As we mentioned before, the propagator $\mathcal{G}(x_T, x|x_0, 0)$ for a given Langevin equation, describing the motion of a particle, is defined as the probability of finding the particle at $x = x_T$ at time $t = T$. Assume the initially particle is positioned at $x(0) = x_0$ at time $t = 0$. Hence, the particle's average motion of over all possible paths that compatible the noise within the boundary conditions $x(0) = x_0$ and $x(T) = x_T$ can indicate the propagator.

The essential effort is to measure probability $\mathcal{P}(\upsilon(t))\mathfrak{D}\upsilon(t)$ on the space of maps $\upsilon(t)$: $[0,T] \to \mathbb{R}$. Due to the uncorrelation of the process $\upsilon(t)$ with the time and its

being distributed as Gaussian for each time t, the probability measurement can be defined as

$$\mathcal{P}(v(t))\mathfrak{D}v(t) = \exp\left(-\frac{1}{2}\int_0^T v(t)^2 \mathrm{d}t\right)\mathfrak{D}v(t). \tag{2.53}$$

In order to obtain the propagator of the equation (2.51), we can claim that the boundary conditions x_0 and x_T can be employed in the following constraint on the process $v(t)$, that is given by

$${}_0\mathcal{D}_T{}^{-(H+\frac{1}{2})}[v] = x_T - x_0. \tag{2.54}$$

Therefore, the propagator can be written as the expectation value:

$$\mathcal{G}(x_T, T|x_0, 0) = \int \delta\left({}_0\mathcal{D}_T{}^{-(H+\frac{1}{2})}[v] - (x_T - x_0)\right)\exp\left(-\frac{1}{2}\int_0^T v(t)^2 \mathrm{d}t\right)\mathfrak{D}v(t). \tag{2.55}$$

In this equation, the Dirac delta function restricts the maps of $v(t)$ so that the integration takes a part on the maps that satifies the constraint in the equation (2.54). To compute the path integral of the right hand side of the propagator equation (2.55), the associated action will be defined as

$$\mathcal{S}[v(t)] = \frac{1}{2}\int_0^T v(t)^2 \mathrm{d}t \tag{2.56}$$

and presume the infinitesimal variatons on the constraint (2.54) compatible maps of $v(t)$. Using a change of variables provides a clear illustration of the parameters making action both stationary and varying. For the parameter that makes the action stationary $v_{st}(t)$ and for varying parameter $\varepsilon(t)$ will be assigned and then, the consequent function becomes $v(t) = v_{st}(t) + \varepsilon(t)$. Notice that the stationary parameter for the action satisfies the constraint of the motion (2.54). If we substitute the new form of the

equation into the constraint, one gets this result

$$ {}_0\mathcal{D}_T^{-(H+\frac{1}{2})}[\varepsilon] = 0 \tag{2.57} $$

Then, it can easily be claimed that the action has a quadratic form in $\upsilon(t)$ and $\upsilon_{st}(t)$ makes it stationary. Using this fact one can rewrite the propagator as

$$ \mathcal{G}(x_T, T|x_0, 0) = e^{\mathcal{S}[\upsilon_{st}(t)]} \int \delta \left({}_0\mathcal{D}_T{}^{-(H+\frac{1}{2})}[\varepsilon] \right) e^{\mathcal{S}[\varepsilon(t)]} \mathfrak{D}\varepsilon(t) \tag{2.58} $$

then, the equation can be worked out to a new form

$$ \mathcal{G}(x_T, T|x_0, 0) = f(T) e^{\mathcal{S}[\upsilon_{st}(t)]}. \tag{2.59} $$

The function $f(T)$ will be computed later on, first imposing the normalization conditions on the propagator gives

$$ \int_{-\infty}^{\infty} \mathcal{G}(x_T, T|x_0, 0) \mathrm{d}x_T = 1, \quad \forall T. \tag{2.60} $$

Now, we will deal with calculating the stationary points of $\mathcal{S}[\upsilon(t)]$ bound by the constraint (2.54). The direct solution for this constraint needs difficult calculations. To avoid these hard computations and resolve this issue easily, we will use the Langrange multipliers. The problem seems similar to finding the stationary points of

$$ \hat{\mathcal{S}}[\upsilon(t), \lambda] = \frac{1}{2} \int_0^T \upsilon(t)^2 \mathrm{d}t + \lambda \left({}_0\mathcal{D}_T^{-(H+\frac{1}{2})}[\upsilon] - (x_T - x_0) \right), \tag{2.61} $$

under *arbitrary* infinitesimal variations of $\upsilon(t)$ and the Lagrange multiplier $\lambda \in \mathbb{R}$. From variations over λ,

$$ \delta_\lambda \hat{\mathcal{S}}[\upsilon(t), \lambda] = \delta\lambda \left({}_0\mathcal{D}_T^{-(H+\frac{1}{2})}[\upsilon] - (x_T - x_0) \right), \tag{2.62} $$

we recover, of course the constraint (2.54)

$$ {}_0\mathcal{D}_T^{-(H+\frac{1}{2})}[v_{st}(t)] = x_T - x_0. \tag{2.63} $$

Then, from the variations in $v(t)$:

$$ \delta_v \hat{\mathcal{S}}[v(t), \lambda] = \int_0^T v(t)\delta v(t)\mathrm{d}t + \lambda_0 \mathcal{D}_T^{-(H+\frac{1}{2})}[\delta v]. \tag{2.64} $$

The explicit for of the fractional integral is

$$ \begin{aligned} \lambda_v \hat{\mathcal{S}}[v(t), \lambda] &= \int_0^T v(t)\delta v(t)\mathrm{d}t + \frac{\lambda}{\Gamma(H+\frac{1}{2})}\int_0^T (T-t)^{H-\frac{1}{2}}\delta v(t)\mathrm{d}t \\ &= \int_0^T \left(v(t) + \frac{\lambda}{\Gamma(H+\frac{1}{2})}(T-t)^{(H-\frac{1}{2})} \right) \delta v(t)\mathrm{d}t. \end{aligned} \tag{2.65} $$

Since $\delta_v \hat{\mathcal{S}}[v(t), \lambda]$ should disappear for random $\delta v(t)$, we find

$$ v_{st}(t) + \frac{\lambda}{\Gamma(H+\frac{1}{2})}(T-t)^{(H-\frac{1}{2})} = 0. \tag{2.66} $$

The Lagrange multiplier λ is found by applying ${}_0D_T^{-(H+\frac{1}{2})}$ to the last equation (2.66) and using the equation (2.63), we get

$$ x_T - x_0 + \frac{\lambda}{\Gamma^2(H+\frac{1}{2})}\int_0^T (T-t)^{(2H-1)}\mathrm{d}t = 0. \tag{2.67} $$

After performing the integration, we find

$$ x_T - x_0 + \frac{\lambda}{\Gamma^2(H+\frac{1}{2})}\frac{T^{2H}}{2H} = 0, \tag{2.68} $$

and

$$ \lambda = -2H\Gamma^2\left(H+\frac{1}{2}\right)\frac{x_T - x_0}{T^{2H}} = 0 \tag{2.69} $$

Substituting this into (2.66):

$$\upsilon_{st}(t) = 2H\Gamma\left(H+\frac{1}{2}\right)\frac{x_T - x_0}{T^{2H}}(T-t)^{H-\frac{1}{2}}. \tag{2.70}$$

The propagator equation in (2.59) becomes

$$\mathcal{G}(x_T, T|x_0, 0) = f(T)\exp\left(H\Gamma^2\left(H+\frac{1}{2}\right)\frac{(x_T - x_0)^2}{T^{2H}}\right). \tag{2.71}$$

Now, we can impose the normalization condition of the propagator in (2.60) and we find $f(T)$ as

$$f(T) = \sqrt{\frac{H}{\pi}}\frac{\Gamma\left(H+\frac{1}{2}\right)}{T^H}. \tag{2.72}$$

Then, we substitute the last expression into the propagator (2.59)

$$\mathcal{G}(x_T, T|x_0, 0) = \sqrt{\frac{H}{\pi}}\left(\frac{\Gamma\left(H+\frac{1}{2}\right)}{T^H}\right)\exp\left(H\Gamma^2\left(H+\frac{1}{2}\right)\frac{(x_T - x_0)^2}{T^{2H}}\right). \tag{2.73}$$

Finally, we derived the general propagator for the fBm. If we define $H = \frac{1}{2}$, we end up with the propagator of the Brownian motion (2.48) with $D_0 = \frac{1}{2}$

$$\mathcal{G}(x_T, T|x_0, 0) = \sqrt{\frac{1}{2\pi T}}\exp\left(-\frac{(x_T - x_0)^2}{2T}\right) \tag{2.74}$$

After all these computations, we achieved our purpose, to find a general propagator that describes all the processes including sub-diffusive and super-diffusive motions. Now, we can take a final step by constructing the kinetic equation for the corresponding process or fBm. To begin with, let us take the Fourier transform of the propagator $G(x_T, T|x_0, 0)$ with respect to x as a trick in obtaining the kinetic equation and then

the transformation yields

$$\hat{\mathcal{G}}(k,t) = \exp\left(-\frac{t^{2H}}{4H\Gamma^2(H+\frac{1}{2})}k^2\right). \tag{2.75}$$

Taking the time derivation of this transform gives us

$$\frac{\partial\hat{\mathcal{G}}(k,t)}{\partial t} = -\frac{t^{2H-1}}{2\Gamma^2(H+\frac{1}{2})}k^2\hat{\mathcal{G}}(k,t). \tag{2.76}$$

To get the kinetic equation out of the above expression (2.76), we perform inverse Fourier transform and, finally, we end up with the kinetic equation:

$$\frac{\partial\mathcal{G}(x,t)}{\partial t} = \frac{t^{2H-1}}{2\Gamma^2(H+\frac{1}{2})}\frac{\partial^2\mathcal{G}(x,t)}{\partial x^2} \tag{2.77}$$

which is also the diffusion equation with time dependent diffusivity, regarding the diffusion constant as $D_0 = \frac{1}{2}$. Wang and Lung derived this equation originally in their paper [63] by using the arguments that based on the fluctuations-dissipation theorem. The invariance of the final equation (2.77) can be easily shown under the transformation $(x,t) \to (a^H x, at)$. Clearly, when we set the Hurst index $H = \frac{1}{2}$ we can extract the normal diffusion equation for the corresponding Brownian motion:

$$\frac{\partial\mathcal{G}(x,t)}{\partial t} = D_0\frac{\partial^2\mathcal{G}(x,t)}{\partial x^2} \tag{2.78}$$

2.5. Diffusion in MRI

2.5.1. Diffusion Weighted MRI

When it comes to investigating the MRI in vivo environment, diffusion imaging is the very first that comes to mind, generating MR images of tissues tuned into the local diffusive features of the molecules. *Diffusion weighted imaging* (DWI) is an MRI technique based upon the diffusive motion of water molecules within tissue voxel. The

random motion of the molecules in water is utilized in MRI acquisition to generate contrast between tissues of an interested region in the body. The sophisticated framework of the diffusion MRI arises from its contrast mechanism at a microscopic level. In T_1-weighted images, application of a strong magnetic field triggers simultaneous precession of protons of water molecules in a sample that yields MR signal. In T_2-weighted images, the measurement of the loss of coherence or synchrony between the protons within a sample of water molecules produces the image contrast. In vivo environments, due to the liquidity of the region, the relaxation process takes a long time which can be beneficial in some clinical cases so that there might be a contrast difference between a healthy tissue and a pathologic one.

To intensify the sensitivity of diffusion in MR images, spatially dependent pulsed field gradients are applied which triggers precession of protons at different frequencies resulting in phase dispersion and signal loss. To initiate the refocusing or rephasing process, the initial gradient is applied second time in the opposite direction. The net gradient field becomes zero with the application of zero; however, due to the movement of the protons during the time interval between pulse applications, the acquired net phase might not be neutralized and that causes an attenuation in the measured MR signal. This *pulse field gradient* technique was firstly performed by Stejskal and Tanner [9] who discovered the signal attenuation arisen from the application of gradient fields in respect to the diffusion of the protons. The signal measurement regarding the diffusivity and the delay between two pulses is given by

$$S(T_E) = S_0 \exp\left[-\gamma^2 G^2 \delta^2 \left(\Delta - \frac{\delta}{3}\right)\right] \tag{2.79}$$

where S is the diffusion weighted signal, S_0 is the signal measured without diffusion effect, γ is the gyromagnetic ratio, G is the magnitude of the gradient field, δ is the time of pulse application, Δ is the delay between two pulses, and lastly, D is the diffusivity constant.

To localize the attenuation of the signal, Stejskal and Tanner suggested that combining the pulsed magnetic gradient fields with additional “motion-probing” gradient

fields because of the incapacity of pulsed gradient fields at producing diffusion related signal attenuation. The combination of pulses is very tricky due to the emanation of the cross-terms between gradient fields, and then, the signal equation (2.79) derived by the Stejskal and Tanner becomes inaccurate. In 1884, to overcome this problem, Le Bihan, a Ph.D. student in physics, suggested a solution that was representing all gradient terms as a *b-factor* (which is entirely subjected to the acquisition parameters). Consequently, the equation (2.79) for the signal attenuation becomes [14]

$$S(T_E) = S_0 \exp\left(-b.\tilde{D}\right) \tag{2.80}$$

$$b = \gamma^2 G^2 \delta^2 \left(\Delta - \frac{\delta}{3}\right) \tag{2.81}$$

where $\tilde{D}$ represents the apparent diffusion coefficient (ADC). A diffusion process in tissues is restricted by boundaries of a region, modulated by the surrounding obstacles and also effected by *Intravoxel Incoherent Motion* (IVIM) such as CSF fluid in ventricles and blood flow in microscopic vessels causing an attenuation of the signal. In addition, DWI measurements requires relatively long T_E times resulting in significant amount of T_2 weighting in the images. The signal attenuation in an image determined by a large b value and long T_E relaxation time might be a result of either tissues with long T_2 relaxation times, restricted diffusive motion (or small ADC), or both of them. Lastly, the directional dependence of the diffusion can cause loss of DWI weighting. To be precise, diffusivity D is equal in all directions in pure solutions that is referred as isotropic diffusion. However, diffusion is generally anisotropic in tissues meaning that the diffusivity or ADC differs from a direction to another. To overcome this problem, a mathematical representation is utilized, tensor notation, which represents the diffusion as a 3×3 matrix.

Although, reducing the voxel size by utilizing high spatial resolution methods can diminish the effects of IVIM. This process costs an extensive amount of scan time to obtain sufficient SNR, which is not preferred and thus is not used. In biological systems, the IVIM process is dramatically faster than the diffusion process thus, it can be ruled out by performing higher gradient fields sensitized the diffusion or by

utilizing the biexponential function of the encoding strength as a model for the signal attenuation.

A better ADC measurement can diminish the T_2 effects. To achieve this reduction, generating images with different b values distinguish the pure diffusion maps or ADC maps where the diffusion is sole contrast source.

Two methods can be used for reducing the directional dependence of diffusion; a trace image acquisition and diffusion tensor imaging (which will be discussed in detail in next section). The trace image is produced by taking an average of the diffusion occurring in a tissue voxel at a certain b value in three directions. This approach, the trace image approach, has an invariance of the gradient direction. This provides the usage of three gradient directions (G_x, G_y, G_z). In addition, the trace image provides a good estimation of overall diffusion occurring in the tissue; yet, the directional information of the molecular motion will be ignored.

2.5.2. Diffusion Tensor Imaging

Diffusion tensor imaging (DTI) is another methodology for diffusion MRI that determines the restricted water diffusion in a tissue. This technique is generally utilized for imaging the brain, especially, to depict the neural network tracking in the brain. In addition to brain, DTI provides a significant morphologic information about muscle types, and other tissues such as prostate [64]. In such biological environments, diffusion happens anisotropically meaning that diffusion processes in one preferential direction. Hence, the diffusion measurement in one gradient direction would not be equal to the measurement in another gradient direction.

To calculate the preferential directions for diffusion, two gradient pulses consisting of all gradient pairs ($G_x - G_x$, $G_x - G_y$, $G_y - G_z$, etc.) are used in the signal measurements. To calculate the diagonal terms of the diffusion tensor, one can make a measurement with the gradient direction (G_x) in the same direction (G_x), whereas the measurements made within different directions, ($G_x - G_y$, $G_z - G_y$, etc.) generates the

off-diagonal terms of the tensor. To determine the preferred diffusion direction(s), the eigenvalues of the tensor matrix must be calculated. In other words, the diagonalization of the tensor matrix gives the preferred directions for the diffusion. The eigenvectors of the diagonalized tensor matrix, D_{diag}, corresponds to these preferred directions and the eigenvalues represent the ADC value for the corresponding direction.

The eigenvector basis to define the directions for diffusion is frequently used in measurements since it is the simplest diffusion representation. To visualize the anisotropic diffusion, a 3D ellipsoid is used in the presentation whose axes correspond to the preferred direction or eigenvector for diffusion and whose size in a given axis is proportional to the square root of the eigenvalue (or ADC) of the corresponding direction. On the other hand, a sphere is used to model isotropic diffusion having equal eigenvalues in all three directions. In anisotropic diffusion tensor, all eigenvalues or one of them can be different. In the first scenario, the ellipsoid will have different length sizes in three directions, whereas the latter case will have an ellipsoid with two directions equal in length. The longest direction of the ellipsoid, which is the largest eigenvalue or ADC, determines the principal direction for the diffusion.

Another approach for determining diffusion anisotropy is considering the diffusion tensor in two parts; the part containing isotropic components of the diffusion (D_{iso}) and the other part containing anisotropic components of the diffusion (D_{aniso}). These parts can be computed by the anisotropic component. The ratio of these components gives the relative anisotropy (RA):

$$RA = \frac{D_{aniso}}{D_{iso}}, \tag{2.82}$$

while the ratio of the anisotropy component to the diagonal representation gives the fractional anisotropy (FA):

$$FA = \left(\frac{3}{2}\right)^{\frac{1}{2}} \frac{D_{aniso}}{D_{diag}} \tag{2.83}$$

In isotropic diffusion case, both quantities become zero. Also, to differentiate the components, coloring is used with each direction having different color (**x**: red, **y**: green, **z**: blue).

2.5.3. q-Space Imaging

In diffusion MRI, a method, known as q-space, is used to process acquired image data, analogous to the conventional method k-space. q-Space is a 3D space with coordinates defined by a vector **q**. The application of a single pulsed gradient field generates a diffusion weighted image that corresponds a point in q-space. In other words, the diffusion signal intensity is stored in the q-space as a particular position q for each tissue position. Data sampling in q-space can be achieved through the repeated applications of different amplitude and direction of gradient fields. Like in the k-space, the data in q-space is also subjected to the Fourier transformation. Performing Fourier transformation to the q-space data yields a diffusion probability density function which is referred as the ensemble average propagator (EAP). The idea of q-space imaging was brought about by Callaghan [65] similar to the k-space methodology. The k-space utilizes the readout gradient (G_{RO}) in the encoding process of the data, while q-space uses the diffusion sensitized gradient or diffusion gradient G_{DIFF}. The Fourier transformation of the k-space signal gives the spatial data of the spin distribution, whereas the Fourier transformation of q-space signal yields the EAP.

$$S(\mathbf{q}) = \int P(\mathbf{r}) e^{-i\mathbf{q}\cdot\mathbf{r}} \mathrm{d}\mathbf{r} \tag{2.84}$$

where $S(\mathbf{q})$ represents the q-space signal and $P(\mathbf{r})$ is the diffusion probability density function (or EAP). The equation above can give an estimation of EAP meaning that an estimation of diffusion environment in spite of its heterogeneity. The value of **q** can be calculated with this relation:

$$\mathbf{q} = \gamma \mathbf{G} \delta \tag{2.85}$$

where δ is the time for application of gradient field $\mathbf{G}$.

Varying the diffusion time interval or the delay Δ between two gradient pulses provides a sampling of q-space and an enhancement in different properties. To acquire better spatial resolution, a longer diffusion time interval can be used. For example, the diffusion within an axis of a neuron; for a short time of diffusion, the amount of diffusion in each direction will be similar, whereas in a long time interval, the diffusion in the long axis of the axon will be distinguished. Hence, a long time interval diversifies the signal in different directions; however, it can cause a lower SNR value.

Due to the definition of the b-value, which is proportional to the square of the q value and the diffusion time interval Δ, it can be used to describe the parameters used in q-space sampling. All diffusion weighted images require a base image in which diffusion is not weighted ($q = 0$ and $b = 0$) in order to compare them.

3. SIMULATIONS AND RESULTS

In this section, the aim of our simulations, what we wanted to achieve, how they were modeled in a computer environment, and the results gathered from them will be discussed. To begin with, it would be great to mention that all the simulations were conducted or modeled using Python programming language. Since, Python is very expedient interpreted language, easy-to-code and involving numerous open source libraries the choice of this language facilitated our efforts on modeling our simulations. The features of this programming language helped us in numerous areas such as in debugging errors, mathematical calculations, clear and perceivable coding, etc. The physics behind the simulations enabled us to perform them in one dimension (1D). With the gradient sequences, two dimensions can be eliminated since when you apply a gradient sequence on the z-axis, only the movement performed on this axis contributes the phase acquired from the random movement of the particles in three-dimensional (3D) space, because of the dot product when measuring the phase. The other angles of the movement yield no phase. Using this fact of the MRI acquisition provides convenience to conduct the simulations in 1D.

The main objective, in our simulations, is to extract MRI signal from the particles diffusing under a variety of conditions which will be discussed in detail. In generally, the particles perform a random walk motion for a particular time at room temperature while experiencing an external magnetic field and gradient sequences. Throughout their movement, they gain a certain phase that helps us to measure the signal gathered from a simulation. Briefly, we introduced a Hookean force to restrict the diffusive motion of the particles to inspect its effects in various conditions on the MRI signal; then, as a further step to previous simulation, we trapped all the particles in a confined space by using different potentials to observe their behavior whether they act as a boundary of the space.

To design the simulations that we conducted, firstly, Monte Carlo approach is required for the stochastic movement of the particles. Each particle moves randomly

at each step, in order to provide that stochasticity we generate a pseudo number to determine the probability of the going right or left. This process is a principle approach in the simulation which is used in a similar manner for all simulations. While these particles are moving, the gradient sequences are performed to measure the accumulated phase on the particles. After the movement of the particles is completed, a signal measurement can be executed. In the simulation section, firstly, a discussion will be held for the details of Monte Carlo technique for each simulation. Then, the implementations and the results for each simulation will be introduced. Firstly, we will study the MR signal for particles restricted by a Hookean force and then, we will restrict the particles by using quadratic potentials ($\propto x^2$, $\propto x^4$, and $\propto x^6$) and infinite well potentials with adhesion effect on the walls (stickiness: 0, 0.9, and 0.99 out 1). For these simulations, after the measurement of the MR signal, by performing Fourier analysis on the signals, we will try to recover the potentials introduced to check that whether these potentials define the corresponding boundaries for the particles trapped within them. Finally, we will present the results obtained from each simulation.

3.1. NMR signal measurement in the presence of a Hookean force

In this section, we will present the implementation and results of our simulation which was the NMR signal extracted from the particles diffusing under the influence of a Hookean force. The goal of this simulation is to observe the variation of NMR signal of the particles that are restricted in movement. In one dimensional domains, the restriction would be boundaries at certain two points. To model this square well potential, we introduce a Hookean potential that might behave as the square well potential (Figure: 3.1). The effect of the Hookean force or the restriction, experienced by the diffusing particles, on the NMR signal will be investigated within different scenarios. Firstly, we will execute a simulation with Stejskal and Tanner pulse sequence [9], and then we employ an oscillatory (sinusoidal) pulse sequence [66] to observe the NMR signal attenuation. The analytical computations of the simulations will be briefly discussed as a review of our recent paper [18], in which the theoretical computations were performed by Cem Yolcu and the multiple correlation function (MCF) formalism

was implemented by Muhammed Memiç. We will include the signal measurement for both Stejskal-Tanner pulse sequence and the oscillating gradient waveforms.

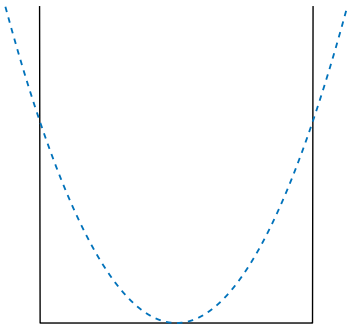

Figure 3.1. Hookean potential profile as a model for square well potential in 1D

3.1.1. Path Integral Formalism

A general average signal, extracted from diffusing particles that experience a spatially dependent magnetic field gradient of duration T_d, can be expressed as

$$E = \left\langle \exp\left(-i\gamma \int_0^{T_d} \mathrm{d}t \mathbf{G}(t) \cdot \mathbf{r}(t)\right)\right\rangle . \tag{3.1}$$

The expectation value of the average signal can be computed through a path integration over all realization paths with a probability weight on each path $\mathbf{r}(t)$. Notice that the signal value E is normalized when $\mathbf{G} = 0$. The probability weight can be considered as an infinite product of step-wise transition probabilities from one path to the another. We presume that the process of particles' movement on the stochastic trajectories is a diffusion process with diffusivity D_0 under the influence of a dimensionless Hookean potential,

$$V(\mathbf{r}) = \frac{1}{2}\mathbf{r}^T\mathbf{C}\mathbf{r} \tag{3.2}$$

where $\mathbf{C}$ is the *confinement tensor* having the units of an inverse of square length. The multiplication of $\mathbf{C}$ with the Boltzmann constant k_B and temperature T gives the tensor for the Hookean force constant. The potential defined above is presumed to

be sufficient to describe the behavior of the diffusing particles in a confined spaces. After an algebraic computation, we derived that if an arbitrary gradient field ($\mathbf{G}(t)$) is applied, the resultant NMR signal is given by

$$E = \exp\left(-D_0 \int_0^{T_d} \mathrm{d}t |\mathbf{Q}(t)|^2 - \frac{D_0}{2}\mathbf{Q}^T(0)\mathbf{\Omega}^{-1}\mathbf{Q}(0)\right) \tag{3.3}$$

where $\mathbf{Q}(t)$ is defined as

$$\mathbf{Q}(t) = \gamma \int_t^{T_d} \mathrm{d}t' e^{-\mathbf{\Omega}(t'-t)}\mathbf{G}(t') \tag{3.4}$$

and the matrix $\mathbf{\Omega}$ is

$$\mathbf{\Omega} = D_0\mathbf{C} \tag{3.5}$$

a matrix of rate constant having the dimensions of inverse time (s^{-1}) that is proportional to the confinement tensor $\mathbf{C}$. By checking through the inverse of this matrix, we can control whether the distribution of the particles approaches to the Boltzmann distribution ($\sim e^{-V(\mathbf{r})}$) [18]. Hence, it is the finite width of the Gaussian profile that is considered as a measure confinement.

The gradient waveforms that we studied is shown in the figure (3.2) below. Using these waveforms first we computed the NMR signal form for corresponding gradient waveform, algebraically. Later we will discuss the simulations conducted employing these waveforms.

Let us start with the Stejskal-Tanner pulse sequence [9], shown in the figure (3.2-a), two gradient pulses in opposite directions with diffusion time interval Δ between pulses. The magnitude of each pulse is G and the duration of them is defined to be δ.

The NMR signal computation using this path integral formalism is given in detail in the article [18]. The resultant NMR signal with regarding the confinement tensor

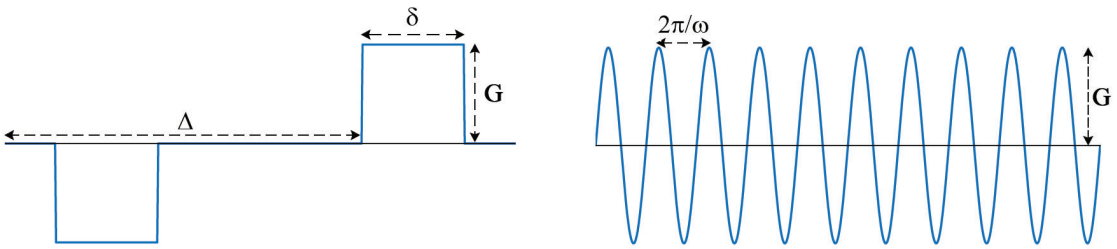

(a) Stejskal and Tanner gradient waveform (b) Oscillatory gradient waveform

Figure 3.2. Gradient Sequence Profiles

for Stejskal-Tanner pulse sequence is expressed as

$$E = \exp -\mathbf{G}^T \mathcal{A} \mathbf{G} \tag{3.6}$$

where the real symmetric matrix is defined as

$$\mathcal{A} = D_0 \gamma^2 \mathbf{\Omega}^{-3} \left[(\mathcal{I} - e^{-\mathbf{\Omega}\Delta})(\mathcal{I} - e^{-\mathbf{\Omega}\delta})^2 e^{\mathbf{\Omega}\delta} - (\mathcal{I} - e^{-2\mathbf{\Omega}\delta}) e^{\mathbf{\Omega}\delta} + 2\mathbf{\Omega}\delta \right]. \tag{3.7}$$

where $\mathcal{I}$ is the 3×3 dimensional unit matrix.

The two expressions above (3.6 and 3.7) can be used as an alternative model to the diffusion tensor model [67, 68]. The main distinction is the dependence of the measured signal on the timing parameters of the sequence. In DTI, this dependence is also valid for free diffusion. In the Hookean potential model, the dependence has coherence with the restricted diffusion [69]. The signal equation to the $\mathcal{O}(\delta^3)$ is given below as a verification

$$\ln E \approx D_0 \gamma^2 \delta^2 \mathbf{G}^T \left(\mathcal{I} - e^{-\mathbf{\Omega}\Delta} - \frac{\Omega\delta}{3} \right) \mathbf{G}, \tag{3.8}$$

which is the same expression with the result of anisotropic generalization, derived by Stejskal [16], for a spherically symmetric harmonic potential with the extra $\mathcal{O}(\delta^3)$ term.

In the limit of inverse time $\Omega \to 0$ (or $C \to 0$), the Stejskal-Tanner expression for free diffusion is restored [9].

In the oscillating gradient case, a sinusoidal waveform, illustrated in the figure (3.2-b), with angular frequency ω is employed. With the help of the involvement of harmonic potential, an analytical expression for the average magnetization for this waveform can be computed. Once more, the algebraic calculations, held by Cem, of the signal can be found explicitly in the paper [18]. The resultant signal expression is given as

$$\frac{\Omega^2+\omega^2}{D_0\gamma^2G^2}\ln E = \frac{\cos\varphi_+\cos\varphi_-}{\Omega}\left(1-e^{-2\pi N\frac{\Omega}{\omega}}\right)-\frac{\pi N}{\omega}, \tag{3.9}$$

where $\cos\varphi_+ = \varphi + \cot^{-1}(\Omega/\omega)$ and $\cos\varphi_- = \varphi - \cot^{-1}(\Omega/\omega)$.

3.1.2. Random Walk Simulations and Results

In our simulations, for each particle, to implement a "free" random walk, generating a pseudo number to assign the probability of going left or right would be enough. However, each particle experiences an attractive potential that manipulating the probability at each position. Due to the potential, the probability of going left or right of a particle differs from $\frac{1}{2}$ depending on the position of the associated particle. In order to measure this variation on the probabilities, let us introduce the biased Bernoulli trials executed at uniform time intervals τ and step length l. The trials are biased in the sense that the probabilities $p_+ = p$ and $p_- = 1-p$ of a particle's movement in $\Delta x = +l$ direction and in the reverse direction $\Delta x = -l$, respectively, are not equal each other due to the presence of a force experienced by the particle. The condition held by the requested diffusive element for such a random motion, corresponding the free diffusion coefficient D_0, can be expressed as

$$D_0 = \frac{l^2}{2\tau} \tag{3.10}$$

Meanwhile, the drift velocity of a random walker, $(p_+ - p_-)l/\tau$ is assumed to be equal to the drift velocity $D_0F/(k_BT)$ of a Brownian particle under the influence of a force F. Therefore, the bias on the particle yields

$$p_+ - p_- = \frac{D_0\tau}{k_BTl}F = \frac{l}{2k_BT}F. \tag{3.11}$$

Using this bias measurement, hence, the probability of a particle's movement of any direction can be determined since the parameters τ and l is defined.

The results for *Stejskal-Tanner pulse sequence*, in the figure (3.3), the NMR signal attenuation is plotted as a function of the delay Δ between pulses at fixed $q = \gamma G\delta$. The gradient is applied for one millisecond ($\delta = 1ms$), and the magnitude of the gradient field is set so that the wave number is $q/2\pi = 100mm^{-1}$. The simulations are done at temperature $T = 310K$ and the free diffusivity is chosen to be $D_0 = 3\mu m^2/ms$. The force constant is set according the value of $C = 0.33\mu m^{-2}$ that yields an effective pore size $L_{eff} = 6\mu m$ similar to the size of a red blood cell [18]. The step-length l taken by the particle at each time-step $\tau = \frac{l^2}{2D_0} = 1.67\mu s$ is chosen to be $l = 100nm$.

The signal attenuation with respect to increasing diffusion time is pictured faithfully by the MCF implementation and random walk simulations. In the figure (3.3-b), the absolute error is plotted for both MCF formalism and random walk simulations. The MCF seems to be error-free in the PFG waveform due to the pulse sequence being actually piecewise constant.

The *Oscillating-Gradient waveform* results, in the figure (3.4), the results for oscillating gradient waveform is illustrated. In the simulations, the same values for the bulk diffusivity, the temperature and the force constant, consequently the same effective pore size, are used. The phase shift of the gradient waveform is set to be $\varphi = 0$, the corresponding gradient field is $G(t) = G\cos\omega t$ with $G = 1mT/mm$. In these simulation, the gradient field is applied for a fixed total duration 100ms at all frequencies. The variation of the frequencies is chosen as changing the number of full periods (N) within the given time interval. Hence, $N = 1$ represents the lowest

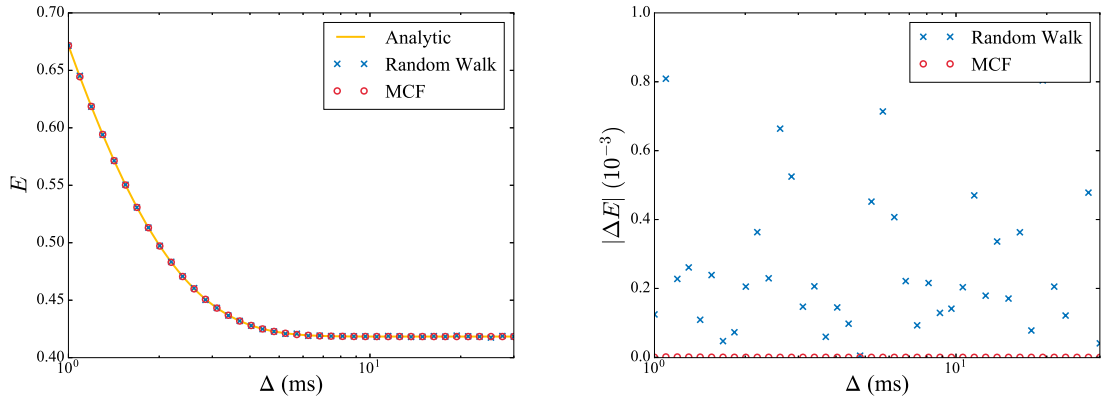

(a) MR signal attenuation (b) The absolute signal error

Figure 3.3. (a):The measured NMR signal plotted vs the gradient pulse separation (diffusion time) in a Stejskal-Tanner pulse sequence. (b): Errors incurred in MCF and random walk results. Plotted values are the absolute values of the deviations from the analytical results.

frequency, whereas the subsequent frequencies are generated by increasing $N = 2, 3, ...$ The MCF results are acquired by the choice of $10\mu s$ time interval. The settings for Stejskal-Tanner simulations are also applied in these simulations.

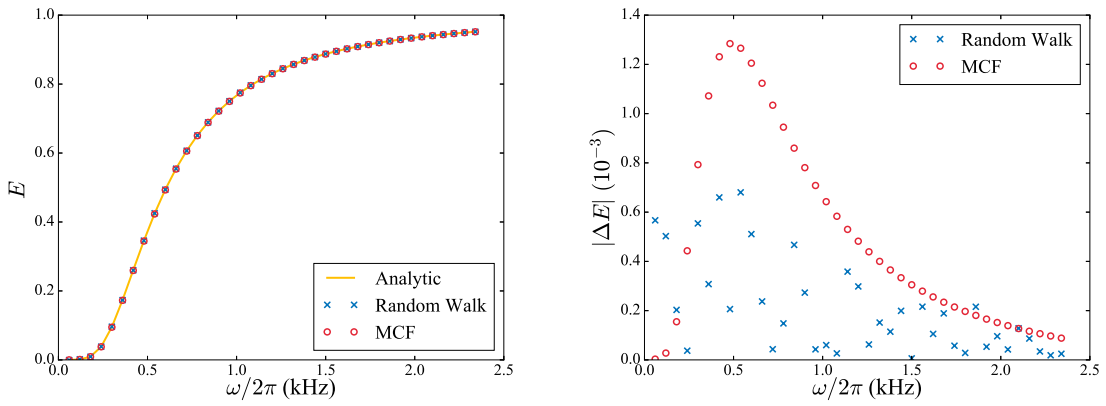

(a) MR signal attenuation (b) The absolute signal error

Figure 3.4. (a): The measured NMR signal plotted vs the frequency in an oscillating gradient sequence. (b): Errors incurred in MCF and random walk results. Plotted values are the absolute values of the deviations from the analytical results

As illustrated in the figure (3.4-a), the frequency dependence of the NMR signal is verified in all three methods; path integral formalism, MCF implementation and ran-

dom walk simulations. The errors in the random walk and MCF simulations, depicted in the figure (3.4-b), contain a smaller range of errors compared to the simulations with Stejskal-Tanner pulse sequence. The errors of the MCF results seem to be advisable since, at low frequency, the error approaches o due to the staircase approximation of the MCF. While the frequency is getting higher, the approximation is deteriorated until a certain point where the period of waveform approaches to the thermalization time scale, $\Omega^{-1} = (D_0 C)^{-1} \simeq 1ms$. The frequencies higher than the neighboring ones, there will be no sufficient for an appreciable diffusion to process in each period of gradient field. Since the diffusion causes the sensitivity of the NMR signal to the inhomogeneities of magnetic field, this hinders the impacts of any misrepresentation of the definite gradient waveform which seems as a decrease in the error with increasing frequency in spite of the relapsing approximation of the MCF formalism. As long as the choice of the time discretization of the MCF is in the appropriate intervals, below the thermalization time, Ω^{-1}, the expected error growth with increasing frequency due to the time discretization is conserved.

The results obtained by the random walk simulations seem promising another perspective of validity of our efforts. The trend of decreasing error with increasing frequency has to be a consequence of statistics. At low frequencies, the particles have a wide range of acquired phase distribution meaning that an accumulated phase of the particle may not be neutralized during the diffusion process. Conversely to that, at high frequencies, a phase acquired by a particle is more probably to be canceled out since, for instance; in the extreme case, at a certain position, the phase acquired may be neutralized at next step of the particle due to the high frequency. The particle might have acquired a positive phase at one step and in the next step particle acquires a negative phase so that the accumulated phase by the particle might be canceled out. Therefore, the lower signal value requires more sampling of phase angle with more walkers and more trajectories. On the other hand, higher frequency values promises a better signal value and a smaller error, in spite of a small number of sampling.

3.1.3. Determination of anisotropy

Combining a force constant tensor, while reserving the diffusivity a scalar, constitutes an alternative characterization of anisotropy for the frequently utilized diffusion tensor model. In this subsection, we will discuss the explicit outcomes for the Stejskal-Tanner sequence, implying the equations (3.6) and (3.7). The diffusion tensor model is expressed as [9, 68]

$$S = \exp\left[-\gamma^2\delta^2\left(\Delta - \frac{\delta}{3}\right)\mathbf{G}^T\mathbf{D}\mathbf{G}\right] \tag{3.12}$$

where $\mathbf{D}$ is the diffusivity tensor. The diffusivity and temperature is chosen as before,

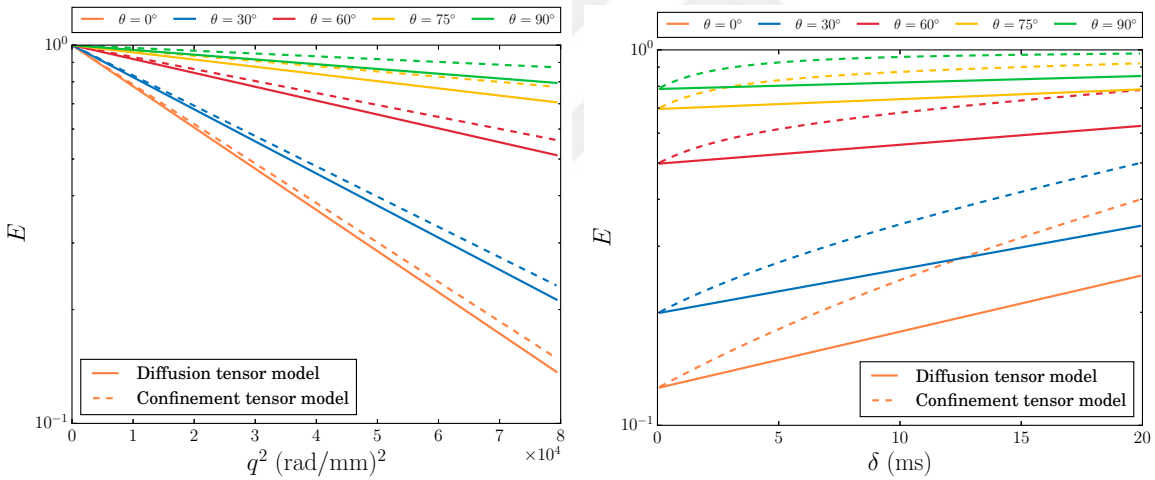

(a) (b)

Figure 3.5. The anticipated MR signal figured vs the square of the angular wavenumber (a) and the pulse duration (b) in a Stejskal-Tanner pulse sequence. Different curves represent different values of the angle (θ) between the gradient vector and the eigenvector of the confinement tensor associated with its smallest eigenvalue

whereas the confinement tensor is defined as diagonal with eigenvalues $C_x = C_y$ so that the relevant pore sizes are approximately $6\mu m$ for C_x and C_y, whereas $C_z = 10C_x$ and the corresponding pore size for C_z is $18\mu m$. The eigenvalues of the diffusion tensor can

be measured by

$$D_i = \frac{1}{C_i \Delta} \left(1 - e^{-C_i \Delta D_0}\right) \tag{3.13}$$

which was determined by the MSD's, $\langle (\Delta x)^2 \rangle$ (check the equation (A6) in the appendix of [18]). The different colors in the figure (3.5) corresponds to different angle values between the gradient direction and the z-axis.

The predicted NMR signal against the square of the angular wavenumber q^2 is depicted in the figure (3.5-1). The diffusion time $\Delta = 20ms$ and the pulse duration $\delta = 2ms$ are configured. Not surprisingly, The linearity q^2 dependence of the signal for both models is illustrated in a semilogarithmic plot. Essentially, the two models give the same results; though, the slight deviation is caused by the pulse duration.

The distinction in the models reveals itself when the pulse duration become a variable of the signal. The dependence of the signal on the pulse duration is plotted as E vs δ in the figure (3.5-b). In this case, the wavenumber is fixed at $q = 90\pi \frac{rad}{mm}$ and the diffusion time $\Delta = 20ms$. As clearly seen in the figure (3.5-b) the diffusion tensor model conserves the linearity in the semilogarithmic plots. However, the dependence in the confinement model seems to be quite complicated, with nonlinearity becoming more significant in the restricted directions.

3.2. Determination of Imaging Energy Landscapes in Diffusion MRI

To investigate the mesoscopic structure of porous media and biological tissue, one can utilize diffusion sensitized gradient fields in NMR experiments. Recently introduced a pulse sequence, shown in the figure (3.6) was asserted to enable performing Fourier transformation to the pore space to be measured [1,2], conversely to the typical gradient pulse sequences that produce only its power spectrum. In other words, the Fourier transformation of the pore space function associated with the usual gradient waveforms yield its own power spectrum. In this simulation we argue that the sequence aforementioned can measure another feature that can be more relevant than the pore

space function in different cases.

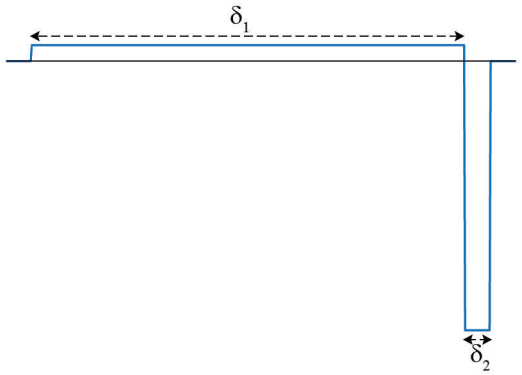

Figure 3.6. The pulse sequence introduced for diffusion pore imaging [1, 2]

To mimic the effects of diffusion in complex media, one can consider the diffusive process under the influence of a potential energy landscape. Through this point of view the inhomogeneities of the media, and also represent boundaries if required, in a more convenient form mathematically. The latter one is for the cases that particles diffusing in a confined space having adhesive boundaries; such processes are presumed to generate diffusion weighted MRI signal sensitive to neuronal activation [70].

The phase ϕ acquired by the particle during the process, $\phi = \gamma\delta\mathbf{G}\cdot\mathbf{r}$, is proportional to the application duration of the gradient pulse δ and the magnitude of the gradient pulse G. The NMR signal sensitized the diffusion is expressed as the expectation value

$$S = \langle e^{-i\phi}\rangle = \left\langle \exp\left(-i\gamma\int_0^{t_f} \mathrm{d}t\mathbf{G}(t)\cdot\mathbf{r}(t)\right)\right\rangle \tag{3.14}$$

of the complex phase acquired by the spin-bearing particles. We employ the Laun's pulse sequence [1, 2] illustrated in the figure (3.6) consisting of a long narrow pulse followed by a short inflated pulse, expressed as a partial function

$$\mathbf{G}(t) = \begin{cases} \mathbf{G} & 0 < t < \delta_1 \\ -\frac{\delta_1}{\delta_2}\mathbf{G} & \delta_1 < t < \delta_1 + \delta_2 = t_f \end{cases} \tag{3.15}$$

When the wavevector q is defined as $q = \gamma\delta_1\mathbf{G}$ and substitute it into the signal equation with the applied pulse sequence, the signal yields the form

$$S = \left\langle e^{-i\mathbf{q}\cdot\left[\int_0^{\delta_1} \mathrm{d}t\mathbf{r}(t)\right]} e^{i\mathbf{q}\cdot\left[\frac{\delta_1}{\delta_2}\int_{\delta_1}^{t_f} \mathrm{d}t\mathbf{r}(t)\right]} \right\rangle \tag{3.16}$$

The integrals in the exponents can be taken into consideration as the center of mass of stochastic trajectories [71]. In the continuum limit where $t_f \to \infty$ and $\delta_2/\delta_1 \to 0$, the long-time limit of time average $1/\delta_1 \int_0^{\delta_1} \mathrm{d}t\mathbf{r}(t)$ must be equal to the statistical average $\langle x \rangle$ that does not depend on time and trajectory. Consequently, the NMR signal equation becomes

$$S(\mathbf{q}) = e^{-i\mathbf{q}\cdot\langle\mathbf{r}\rangle} \left\langle e^{i\mathbf{q}\cdot\mathbf{r}(t)} \right\rangle \tag{3.17}$$

where the simplification of the second phase quantity is the result of the shrinkage in the integration interval to a moment.

The distinction between our purpose and Laun's can be clarified in the underlying diffusion process being under the influence og a potential $V(\mathbf{r})$ rather than the restriction of pore space boundaries. Henceforth, the average position $\langle\mathbf{r}\rangle$ does not resembles the center of mass of the pore space but it is the average position for the corresponding potential landscape. Likewise, the expectation value of the accumulated phase can be computed by the asymptotic ($t_f \to \infty$) probability distribution ($\rho(\mathbf{r}) \sim e^{-\beta V(\mathbf{r})}$), where β is the inverse thermal energy. Consequently, the diffusion MRI signal reveals the Fourier transform of the stationary distribution for the corresponding potential energy landscape. The signal expression for this case involving its mean shifting to the origin can be written as

$$S(\mathbf{q}) = \int \mathrm{d}\mathbf{r}\rho(\mathbf{r}) e^{-i\mathbf{q}\cdot(\mathbf{r}-\langle\mathbf{r}\rangle)} \tag{3.18}$$

where the mean position $\langle\mathbf{r}\rangle$ can be considered as a constant and taken out of the integration. Then the performing the Fourier transformation to the resultant equa-

tion produces the ensemble average propagator or the stationary distribution for the underlying potential landscape.

In the next section, we will argue the validity of our assumption in two distinct cases that re employing quadratic potentials in the diffusion process and manipulating the adhesiveness feature of the boundaries.

3.2.1. Random Walk Simulations and Results

To argue our assumption, we employed three different quadratic potentials ($\propto x^2$, $\propto x^4$, and $\propto x^6$) that restrict the diffusive motion of the particles. We have discussed earlier how a particle moves under the influence of such potentials, the variation in the probability of changing the coordinate Δx or $-\Delta x$ is clearly expressed [18]. In the latter case, we restrict the particles in a one dimensional confined space with adhesive boundaries (with the probability of sticking: 0, 0.9 and 0.99). The particles process a free diffusion in a 1D bounded domain where the restriction imposed on the particles varied by increasing the adhesiveness of the boundaries.

The simulations are held with the parameters that the step-length of a random walker is set to be $l = 100nm$ at each time step $\tau = \frac{l^2}{2D_0} = 1.67\mu s$, in which the free diffusivity constant $D_0 = 3\frac{\mu^2}{ms}$. A sample of $N = 2 \times 10^6$ particles process diffusion at a temperature $T = 310K$. A range of gradient field $G \in [-0.12, 0.12]\frac{mT}{mm}$ is applied to sample the signal data. The mentioned parameter are used for both quadratic potential landscape and adhesive potential landscape simulations. The parameters that are specific to the simulation are the force constant for the quadratic potential landscape, each is chosen so that equilibrium point of the potential ($x = 10\mu m$) and diffusion time is defined to be a sufficient value for each simulation. In the adhesive potential landscape simulations, the particles are trapped in a 1D box of length ($L = 10\mu m$) and the stickiness or the adhesiveness of the boundaries is varied as (0, 0.9, and 0.99). The results are promising and satisfying our assumptions, illustrated in the figures (3.7 and 3.8).

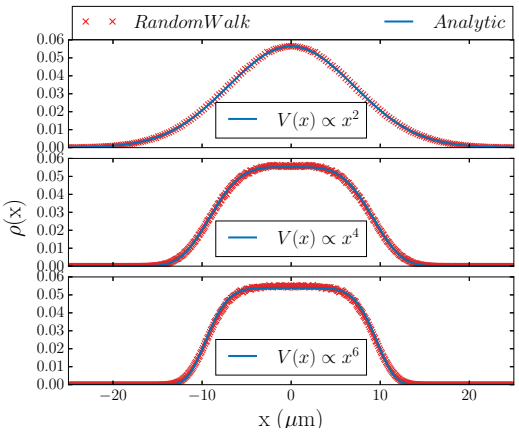

(a) The stationary distributions for the quadratic potential landscapes

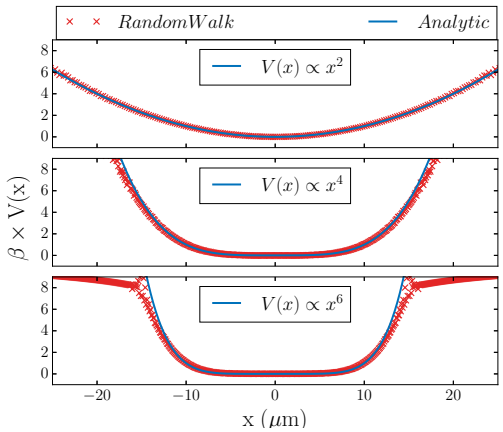

(b) The quadratic potential landscapes

Figure 3.7. Quadratic potential landscapes derived from corresponding stationary distributions at different powers imposed on the diffusion process as a restriction

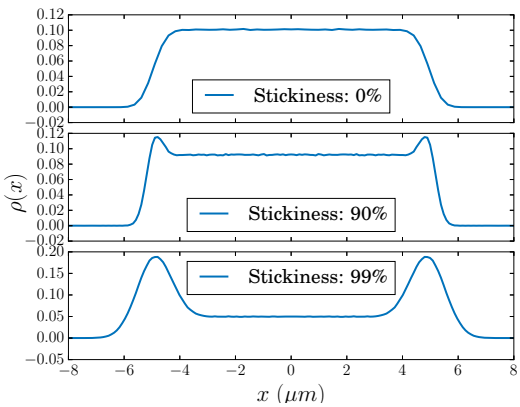

(a) The stationary distributions for the adhesive potential well landscapes

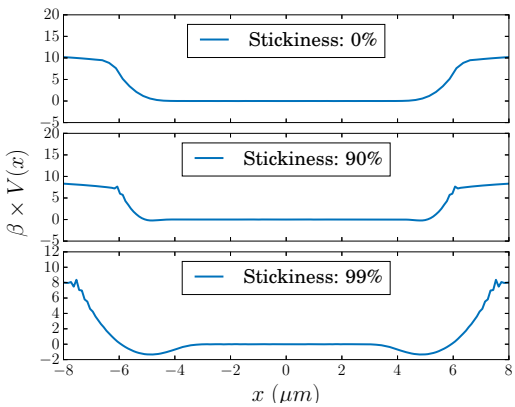

(b) The adhesive potential well landscapes

Figure 3.8. Potential landscapes derived from the stationary distributions at different stickiness levels. The adhesion potential is clearly seen as dips in the landscape in the vicinity of the edges of the box

In the figures labeled as (3.7-a and 3.8-a), the steady state distributions for the corresponding potential landscapes were depicted and in the((3.7-b and 3.8-b) labeled figures, the potential landscapes are plotted.

As illustrated in the figure (3.7), the potentials imposed on the diffusion process and corresponding steady state distributions are measured from the Fourier transformation, discussed previously, of the NMR signal acquired from the process. The measured potentials and steady state distributions resemble the analytic solutions of them. However, there are some off points shown in the figure caused by the simulation parameters. Especially, in the potential $V(x) \propto x^6$ figure, the points around the $\beta V(x) >= 6$ do not match with the analytic solution. This could be arisen from the high stiffness of the potential causing less sampling around the further points and the high q value is required to depict those points correctly. Although, at high q values the signal attenuates rapidly causing more error in the measurements.

In the second case, the adhesiveness is clearly seen as the dips at the boundaries, demonstrated in the figure (3.8). When the adhesive effect increases, the dips in the measured potential landscape deepens. This result is expected, since the adhesiveness of the boundaries resembles an attractive potential near them to trap the particles. The intensity of stickiness of the walls is proportional to the attractiveness of the potential, implying that more particles are trapped for a longer time. The reflecting boundaries (or when the stickiness disappears), shown in the top plots of the figure (3.8) are seen to be a normal square potential well, as expected. The methodology that we suggested seems promising in determining the energy landscape of boundaries.

4. CONCLUSION

Diffusion MRI is very remarkable imaging modality, offering a measurement for water molecules diffusing in microscopical biological structures in vivo. Through the diffusion process that molecules undergo within these regions, areal information associated with the region can be acquired in diffusion NMR experiments. DTI, one of the prominent techniques employed in diffusion NMR experiments, promises to image bounded domain in which water molecules diffuse. The restriction imposed by the boundaries or molecular crowding influence the diffusive motion of the molecules. DTI can provide a phenomenal approach to the restricted water diffusion through defining the diffusivity by a tensor model.

To describe the restriction on the diffusive motion of water molecules, inducing a parabolic potential to the system where the molecules undergo free diffusion is considered to be a better model. The random walkers diffusing under the influence of a Hookean potential is seen to determine the restriction. In the random walk simulations, the usage of parabolic potential as restriction is verified by the analytical results. Our results show that the confinement tensor model [18] seems to an alternative model to the diffusion tensor model. The theoretical approach seems to be confirmed with the random walk and MCF solutions.

In determining the energy landscapes of biological structures, the employment of potentials as a restriction to diffusion or as a boundary property of the region involves substantially promising results. Through diffusion MRI, bulk heterogeneities of a region can be imaged as potential energy landscapes, and also the features of boundaries such as adhesiveness can be determined and mapped by the energy landscapes. However, this technique can be generalized to 3D model so that the more realistic simulations could be performed. Hence, the effects of representing the restrictions as potentials could be comprehended gratifyingly.

REFERENCES

1. Laun, F. B., T. A. Kuder, W. Semmler and B. Stieltjes, "Determination of the defining boundary in nuclear magnetic resonance diffusion experiments", *Physical review letters*, Vol. 107, No. 4, p. 048102, 2011.

2. Laun, F. B., T. A. Kuder, A. Wetscherek, B. Stieltjes and W. Semmler, "NMR-based diffusion pore imaging", *Physical Review E*, Vol. 86, No. 2, p. 021906, 2012.

3. Bottomley, P. A., C. Hardy, R. Argersinger and G. Allen-Moore, "A review of 1H nuclear magnetic resonance relaxation in pathology: Are T1 and T2 diagnostic?", *Medical physics*, Vol. 14, No. 1, pp. 1–37, 1987.

4. Mlynárik, V., S. Gruber and E. Moser, "Proton T1 and T2 relaxation times of human brain metabolites at 3 Tesla", *NMR in biomedicine*, Vol. 14, No. 5, pp. 325–331, 2001.

5. Stanisz, G. J., E. E. Odrobina, J. Pun, M. Escaravage, S. J. Graham, M. J. Bronskill and R. M. Henkelman, "T1, T2 relaxation and magnetization transfer in tissue at 3T", *Magnetic resonance in medicine*, Vol. 54, No. 3, pp. 507–512, 2005.

6. Plewes, D. B. and W. Kucharczyk, "Physics of MRI: a primer", *Journal of magnetic resonance imaging*, Vol. 35, No. 5, pp. 1038–1054, 2012.

7. Yao, B., T.-Q. Li, P. van Gelderen, K. Shmueli, J. A. de Zwart and J. H. Duyn, "Susceptibility contrast in high field MRI of human brain as a function of tissue iron content", *Neuroimage*, Vol. 44, No. 4, pp. 1259–1266, 2009.

8. Rauscher, A., J. Sedlacik, M. Barth, H.-J. Mentzel and J. R. Reichenbach, "Magnetic susceptibility-weighted MR phase imaging of the human brain", *American journal of neuroradiology*, Vol. 26, No. 4, pp. 736–742, 2005.

9. Stejskal, E. O. and J. E. Tanner, "Spin diffusion measurements: spin echoes in the presence of a time-dependent field gradient", *The journal of chemical physics*, Vol. 42, No. 1, pp. 288–292, 1965.

10. Le Bihan, D., E. Breton, D. Lallemand, P. Grenier, E. Cabanis and M. Laval-Jeantet, "MR imaging of intravoxel incoherent motions: application to diffusion and perfusion in neurologic disorders.", *Radiology*, Vol. 161, No. 2, pp. 401–407, 1986.

11. Carr, H. Y. and E. M. Purcell, "Effects of diffusion on free precession in nuclear magnetic resonance experiments", *Physical review*, Vol. 94, No. 3, p. 630, 1954.

12. Özarslan, E. and T. H. Mareci, "Generalized diffusion tensor imaging and analytical relationships between diffusion tensor imaging and high angular resolution diffusion imaging", *Magnetic resonance in Medicine*, Vol. 50, No. 5, pp. 955–965, 2003.

13. Gold, G. E., E. Han, J. Stainsby, G. Wright, J. Brittain and C. Beaulieu, "Musculoskeletal MRI at 3.0 T: relaxation times and image contrast", *American Journal of Roentgenology*, Vol. 183, No. 2, pp. 343–351, 2004.

14. Le Bihan, D. and E. Breton, "Imagerie de diffusion in-vivo par résonance magnétique nucléaire", *Comptes-Rendus de l'Académie des Sciences*, Vol. 93, No. 5, pp. 27–34, 1985.

15. Özarslan, E., T. M. Shepherd, C. G. Koay, S. J. Blackband and P. J. Basser, "Temporal scaling characteristics of diffusion as a new MRI contrast: findings in rat hippocampus", *Neuroimage*, Vol. 60, No. 2, pp. 1380–1393, 2012.

16. Stejskal, E., "Use of spin echoes in a pulsed magnetic-field gradient to study anisotropic, restricted diffusion and flow", *The Journal of Chemical Physics*, Vol. 43, No. 10, pp. 3597–3603, 1965.

17. Karlicek, R. and I. Lowe, "A modified pulsed gradient technique for measuring

diffusion in the presence of large background gradients", *Journal of Magnetic Resonance (1969)*, Vol. 37, No. 1, pp. 75–91, 1980.

18. Yolcu, C., M. Memiç, K. Şimşek, C.-F. Westin and E. Özarslan, "NMR signal for particles diffusing under potentials: From path integrals and numerical methods to a model of diffusion anisotropy", *Physical Review E*, Vol. 93, No. 5, p. 052602, 2016.

19. Smoluchowski, M. V., "Über Brownsche Molekularbewegung unter Einwirkung äußerer Kräfte und deren Zusammenhang mit der verallgemeinerten Diffusionsgleichung", *Annalen der Physik*, Vol. 353, No. 24, pp. 1103–1112, 1916.

20. Uhlenbeck, G. E. and L. S. Ornstein, "On the theory of the Brownian motion", *Physical review*, Vol. 36, No. 5, p. 823, 1930.

21. Fan, Y. and J.-H. Gao, "Fractional motion model for characterization of anomalous diffusion from NMR signals", *Physical Review E*, Vol. 92, No. 1, p. 012707, 2015.

22. Hall, M. G. and T. R. Barrick, "From diffusion-weighted MRI to anomalous diffusion imaging", *Magnetic Resonance in Medicine*, Vol. 59, No. 3, pp. 447–455, 2008.

23. Magin, R. L., O. Abdullah, D. Baleanu and X. J. Zhou, "Anomalous diffusion expressed through fractional order differential operators in the Bloch–Torrey equation", *Journal of Magnetic Resonance*, Vol. 190, No. 2, pp. 255–270, 2008.

24. Bloch, F., "Nuclear induction", *Physical review*, Vol. 70, No. 7-8, p. 460, 1946.

25. Bulte, J. W. and D. L. Kraitchman, "Iron oxide MR contrast agents for molecular and cellular imaging", *NMR in Biomedicine*, Vol. 17, No. 7, pp. 484–499, 2004.

26. Buxton, R. B. and L. R. Frank, "A model for the coupling between cerebral blood flow and oxygen metabolism during neural stimulation", *Journal of Cerebral Blood*

Flow & Metabolism, Vol. 17, No. 1, pp. 64–72, 1997.

27. Haacke, E. M., N. Y. Cheng, M. J. House, Q. Liu, J. Neelavalli, R. J. Ogg, A. Khan, M. Ayaz, W. Kirsch and A. Obenaus, "Imaging iron stores in the brain using magnetic resonance imaging", *Magnetic resonance imaging*, Vol. 23, No. 1, pp. 1–25, 2005.

28. Ogawa, S., T.-M. Lee, A. R. Kay and D. W. Tank, "Brain magnetic resonance imaging with contrast dependent on blood oxygenation", *Proceedings of the National Academy of Sciences*, Vol. 87, No. 24, pp. 9868–9872, 1990.

29. Fick, A., "Ueber diffusion", *Annalen der Physik*, Vol. 170, No. 1, pp. 59–86, 1855.

30. Philibert, J., "One and a half century of diffusion: Fick, Einstein, before and beyond", *Diffusion Fundamentals*, Vol. 4, No. 6, pp. 1–19, 2006.

31. Mandelbrot, B. B. and R. Hudson, *The (mis) behaviour of markets: a fractal view of risk, ruin and reward*, Profile Books, 2010.

32. Einstein, A., "Un the movement of small particles suspended in statiunary liquids required by the molecular-kinetic theory 0f heat", *Ann. d. Phys*, Vol. 17, pp. 549–560, 1905.

33. Von Smoluchowski, M., "Zur kinetischen theorie der brownschen molekularbewegung und der suspensionen", *Annalen der physik*, Vol. 326, No. 14, pp. 756–780, 1906.

34. Einstein, A., *Investigations on the Theory of the Brownian Movement*, Courier Corporation, 1956.

35. Kohlrausch, R., "Nachtrag uber die elastiche Nachwirkung beim Cocon und Glasladen", *Ann. Phys.(Leipzig)*, Vol. 72, No. 393, p. 7, 1847.

36. Williams, G. and D. C. Watts, "Non-symmetrical dielectric relaxation behaviour

arising from a simple empirical decay function", *Transactions of the Faraday society*, Vol. 66, pp. 80–85, 1970.

37. Klafter, J. and M. F. Shlesinger, "On the relationship among three theories of relaxation in disordered systems", *Proceedings of the National Academy of Sciences*, Vol. 83, No. 4, pp. 848–851, 1986.

38. Havlin, S. and D. Ben-Avraham, "Diffusion in disordered media", *Advances in Physics*, Vol. 36, No. 6, pp. 695–798, 1987.

39. Ben-Avraham, D. and S. Havlin, *Diffusion and reactions in fractals and disordered systems*, Cambridge University Press, 2000.

40. Jeon, J.-H., N. Leijnse, L. B. Oddershede and R. Metzler, "Anomalous diffusion and power-law relaxation of the time averaged mean squared displacement in worm-like micellar solutions", *New Journal of Physics*, Vol. 15, No. 4, p. 045011, 2013.

41. Kessler, D. A. and E. Barkai, "Theory of fractional Lévy kinetics for cold atoms diffusing in optical lattices", *Physical review letters*, Vol. 108, No. 23, p. 230602, 2012.

42. Sagi, Y., M. Brook, I. Almog and N. Davidson, "Observation of anomalous diffusion and fractional self-similarity in one dimension", *Physical review letters*, Vol. 108, No. 9, p. 093002, 2012.

43. Bronstein, I., Y. Israel, E. Kepten, S. Mai, Y. Shav-Tal, E. Barkai and Y. Garini, "Transient anomalous diffusion of telomeres in the nucleus of mammalian cells", *Physical review letters*, Vol. 103, No. 1, p. 018102, 2009.

44. Kepten, E., I. Bronshtein and Y. Garini, "Improved estimation of anomalous diffusion exponents in single-particle tracking experiments", *Physical Review E*, Vol. 87, No. 5, p. 052713, 2013.

45. Burnecki, K., E. Kepten, J. Janczura, I. Bronshtein, Y. Garini and A. Weron, "Universal algorithm for identification of fractional Brownian motion. A case of telomere subdiffusion", *Biophysical journal*, Vol. 103, No. 9, pp. 1839–1847, 2012.

46. Regner, B. M., D. Vučinić, C. Domnisoru, T. M. Bartol, M. W. Hetzer, D. M. Tartakovsky and T. J. Sejnowski, "Anomalous diffusion of single particles in cytoplasm", *Biophysical journal*, Vol. 104, No. 8, pp. 1652–1660, 2013.

47. Bickel, D. R., M. T. Verklan and J. Moon, "Detection of anomalous diffusion using confidence intervals of the scaling exponent with application to preterm neonatal heart rate variability", *Physical Review E*, Vol. 58, No. 5, p. 6440, 1998.

48. Allegrini, P., M. Barbi, P. Grigolini and B. J. West, "Dynamical model for DNA sequences", *Physical Review E*, Vol. 52, No. 5, p. 5281, 1995.

49. Allegrini, P., M. Buiatti, P. Grigolini and B. J. West, "Non-Gaussian statistics of anomalous diffusion: The DNA sequences of prokaryotes", *Physical Review E*, Vol. 58, No. 3, p. 3640, 1998.

50. Kenkre, V., E. Montroll and M. Shlesinger, "Generalized master equations for continuous-time random walks", *Journal of Statistical Physics*, Vol. 9, No. 1, pp. 45–50, 1973.

51. Vlahos, L., H. Isliker, Y. Kominis and K. Hizanidis, "Normal and anomalous diffusion: A tutorial", *arXiv preprint arXiv:0805.0419*, 2008.

52. Varotsos, P., N. Sarlis and E. Skordas, "Long-range correlations in the electric signals that precede rupture", *Physical Review E*, Vol. 66, No. 1, p. 011902, 2002.

53. Wu, X.-L. and A. Libchaber, "Particle diffusion in a quasi-two-dimensional bacterial bath", *Physical review letters*, Vol. 84, No. 13, p. 3017, 2000.

54. Bouchaud, J.-P. and A. Georges, "Anomalous diffusion in disordered media: sta-

tistical mechanisms, models and physical applications", *Physics reports*, Vol. 195, No. 4-5, pp. 127–293, 1990.

55. Hurst, H., "Long Term Storage Capacity of Reservoirs", *Transactions of the American Society of Civil Engineers*, Vol. 116, pp. 770–799, 1951.

56. Mandelbrot, B. B. and J. W. Van Ness, "Fractional Brownian motions, fractional noises and applications", *SIAM review*, Vol. 10, No. 4, pp. 422–437, 1968.

57. Perrin, E., R. Harba, C. Berzin-Joseph, I. Iribarren and A. Bonami, "nth-order fractional Brownian motion and fractional Gaussian noises", *IEEE Transactions on Signal Processing*, Vol. 49, No. 5, pp. 1049–1059, 2001.

58. Oldham, K. and J. Spanier, *The fractional calculus theory and applications of differentiation and integration to arbitrary order*, Vol. 111, Elsevier, 1974.

59. Podlubny, I., *Fractional differential equations: an introduction to fractional derivatives, fractional differential equations, to methods of their solution and some of their applications*, Vol. 198, Academic press, 1998.

60. Sebastian, K., "Path integral representation for fractional Brownian motion", *Journal of Physics A: Mathematical and General*, Vol. 28, No. 15, p. 4305, 1995.

61. Decreusefond, L. *et al.*, "Stochastic analysis of the fractional Brownian motion", *Potential analysis*, Vol. 10, No. 2, pp. 177–214, 1999.

62. Calvo, I. and R. Sánchez, "The path integral formulation of fractional Brownian motion for the general Hurst exponent", *Journal of Physics A: Mathematical and Theoretical*, Vol. 41, No. 28, p. 282002, 2008.

63. Wang, K. and C. Lung, "Long-time correlation effects and fractal Brownian motion", *Physics Letters A*, Vol. 151, No. 3-4, pp. 119–121, 1990.

64. Manenti, G., M. Carlani, S. Mancino, V. Colangelo, M. Di Roma, E. Squillaci and

G. Simonetti, "Diffusion tensor magnetic resonance imaging of prostate cancer", *Investigative radiology*, Vol. 42, No. 6, pp. 412–419, 2007.

65. Callaghan, P. T., *Principles of nuclear magnetic resonance microscopy*, Oxford University Press on Demand, 1993.

66. Stepišnik, J., "Analysis of NMR self-diffusion measurements by a density matrix calculation", *Physica B+ C*, Vol. 104, No. 3, pp. 350–364, 1981.

67. Basser, P. J., J. Mattiello and D. LeBihan, "MR diffusion tensor spectroscopy and imaging", *Biophysical journal*, Vol. 66, No. 1, pp. 259–267, 1994.

68. Basser, P. J., J. Mattiello and D. LeBihan, "Estimation of the effective self-diffusion tensor from the NMR spin echo", *Journal of Magnetic Resonance, Series B*, Vol. 103, No. 3, pp. 247–254, 1994.

69. Özarslan, E. and P. J. Basser, "Microscopic anisotropy revealed by NMR double pulsed field gradient experiments with arbitrary timing parameters", *The Journal of chemical physics*, Vol. 128, No. 15, p. 04B615, 2008.

70. Le Bihan, D., "The 'wet mind': water and functional neuroimaging", *Physics in medicine and biology*, Vol. 52, No. 7, p. R57, 2007.

71. Mitra, P. P. and B. I. Halperin, "Effects of finite gradient-pulse widths in pulsed-field-gradient diffusion measurements", *Journal of Magnetic Resonance, Series A*, Vol. 113, No. 1, pp. 94–101, 1995.

APPENDIX A: APPLICATION

A.1. Classical Fractional Operators

A brief introduction to one dimensional fractional integrals and derivatives will be discussed. The more explicit discussion about fractional calculus can be found in the books [58, 59].

The left and right *Riemann-Liouville* fractional integrals can be defined as ${}_a\mathcal{D}_t^{-\kappa}$ and ${}^b\mathcal{D}_b^{-\kappa}$ of order $\kappa \in \mathbb{R}(\kappa > 0)$. Consider a function $f : \mathbb{R} \to \mathbb{R}$ whose left and right *Riemann-Liouville* fractional integral equations are given by

$$ {}_a\mathcal{D}_t^{-\kappa}[f(t)] := \frac{1}{\Gamma(\kappa)} \int_a^t \mathrm{d}t'(t-t')^{(\kappa-1)} f(t'), \tag{A.1} $$

and

$$ {}^b\mathcal{D}_t^{-\kappa}[f(t)] := \frac{1}{\Gamma(\kappa)} \int_t^b \mathrm{d}t'(t'-t)^{(\kappa-1)} f(t'), \tag{A.2} $$

respectively. $\Gamma(\kappa)$ denotes Gamma function. As for the left and right *Riemann-Liouville* fractional differential operators of order κ are expressed as

$$ {}_a\mathcal{D}_t^{\kappa}[f(t)] := \frac{1}{\Gamma(n-\kappa)} \frac{\mathrm{d}^n}{\mathrm{d}t^n} \int_a^t \mathrm{d}t' \frac{f(t')}{(t-t')^{(\kappa-m+1)}} \tag{A.3} $$

and

$$ {}^b\mathcal{D}_t^{\kappa}[f(t)] := \frac{(-1)^n}{\Gamma(n-\kappa)} \frac{\mathrm{d}^n}{\mathrm{d}t^n} \int_t^b \mathrm{d}t' \frac{f(t')}{(t'-t)^{(\kappa-m+1)}}, \tag{A.4} $$

respectively. Here, m is the integer number satisfying $m-1 \leq \kappa < m$ relation.